



Available online at www.sciencedirect.com

ScienceDirect



Journal of Magnesium and Alloys 9 (2021) 1922–1941

www.elsevier.com/locate/jma

Review

Thermodynamics and kinetics of hydriding and dehydriding reactions in Mg-based hydrogen storage materials

Qian Li^{a,e,*}, Yangfan Lu^a, Qun Luo^b, Xiaohua Yang^{c,d}, Yan Yang^a, Jun Tan^a, Zhihua Dong^a, Jie Dang^a, Jianbo Li^a, Yuan Chen^a, Bin Jiang^a, Shuhui Sun^d, Fusheng Pan^{a,*}

^a National Engineering Research Center for Magnesium Alloys, College of Materials Science and Engineering, Chongqing University, Chongqing 400044, China

^b State Key Laboratory of Advanced Special Steels, Shanghai Key Laboratory of Advanced Ferrometallurgy, School of Materials Science and Engineering, Shanghai University, Shanghai 200444, China

^c Institute of Quantum and Sustainable Technology (IQST), School of Chemistry and Chemical Engineering, Jiangsu University, Zhenjiang, 212013, China

^d Institut National de la Recherche Scientifique-Énergie Matériaux et Télécommunications, Varennes, J3X 1S2, Québec, Canada

^e State Key Laboratory of Mechanical Transmissions, Chongqing University, Chongqing 400044, China

Received 30 September 2021; received in revised form 26 October 2021; accepted 31 October 2021

Available online 1 December 2021

Abstract

Mg-based materials are one of the most promising hydrogen storage candidates due to their high hydrogen storage capacity, environmental benignity, and high Clarke number characteristics. However, the limited thermodynamics and kinetic properties pose major challenges for their engineering applications. Herein, we review the recent progress in improving their thermodynamics and kinetics, with an emphasis on the models and the influence of various parameters in the calculated models. Subsequently, the impact of alloying, composite, and nanocrystallization on both thermodynamics and dynamics are discussed in detail. In particular, the correlation between various modification strategies and the hydrogen capacity, dehydrogenation enthalpy and temperature, hydriding/dehydriding rates are summarized. In addition, the mechanism of hydrogen storage processes of Mg-based materials is discussed from the aspect of classical kinetic theories and microscope hydrogen transferring behavior. This review concludes with an outlook on the remaining challenge issues and prospects.

© 2021 Chongqing University. Publishing services provided by Elsevier B.V. on behalf of KeAi Communications Co. Ltd.

This is an open access article under the CC BY-NC-ND license (<http://creativecommons.org/licenses/by-nc-nd/4.0/>)

Peer review under responsibility of Chongqing University

Keywords: Magnesium-based hydrogen storage materials; Hydriding/dehydriding reactions; Thermodynamics; Kinetic models; Analysis methods.

1. Introduction

With the world experiencing an emergent environmental and energy crisis, reducing carbon dioxide (CO₂) emission has become one of the top priorities for many industries [1,2]. Several strategies have been proposed to curb the CO₂ emissions. While natural resources, such as solar power, wind, geothermal, and tidal energy, are the primary candidates of renewable energies, their environment and time-zone dependent resulted in intermittent, capacity-instable, and unpredictable

features. Accordingly, large-scale energy storage and conversion devices (ESCDs) are needed for the practical applications, because direct use of such unstable energy sources is harmful to current power grid systems [3]. Recently, there is growing consensus that hydrogen (H₂) energies can provide a better energy solution for global warming due to their high energy density, zero CO₂ emission, and diverse renewable energy sources.

To promote the mass application of H₂ energy, it is inevitable to establish the industry chains for H₂ production, purification, storage, and consumption. Among them, hydrogen storage is the most challenging procedure for H₂ transportation and consumption. At present, three major technologies are available for hydrogen storage [4,5], i.e., (1) liquified

* Corresponding author.

E-mail addresses: cqliqian@cqu.edu.cn (Q. Li), fspan@cqu.edu.cn (F. Pan).

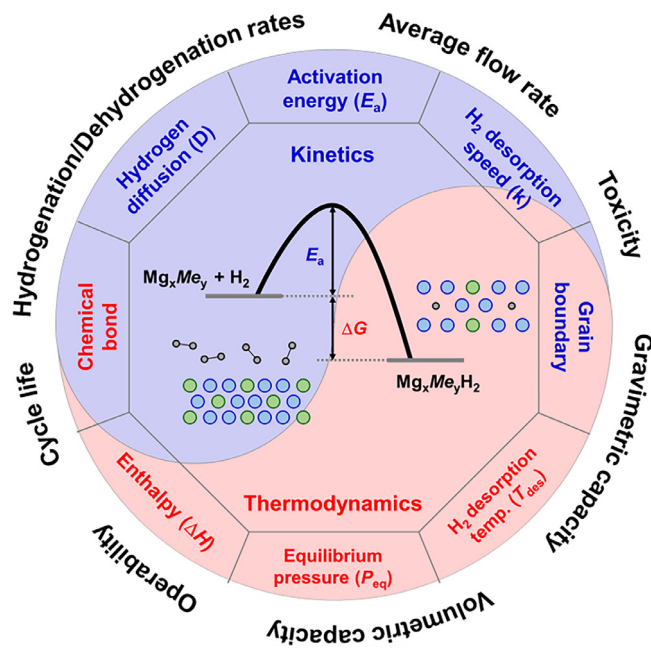


Fig. 1. The relations of thermodynamics and kinetics of hydriding and dehydriding reactions in Mg-based alloys with their hydrogen storage properties.

H_2 in cryogenic tanks, (2) high-pressure gas cylinders, and (3) solid-state H_2 storage technique. Amongst them, solid-state H_2 storage technique has been attracting considerable attention because it is operable under moderate temperatures and nearly ambient pressure condition, realizing higher energy density and improved operability. The first discovery of materials-based H_2 storage was made in 1869 by T. Graham in Pd [6], in which the distance between hydrogen atoms is significantly decreased when the hydrogen atoms are absorbed and coordinated with host materials [7]. Subsequently, major efforts have been devoted to developing extensive hydrogen storage materials due to the low geological reserves of Pd. A milestone breakthrough was achieved in the 1970s represented by the development of non-noble metal materials, such as LaNi_5 and FeTi [8,9]. These materials not only reduce the cost of solid-state H_2 storage but also demonstrate that H_2 can be reversibly absorbed/desorbed under relatively mild reaction conditions [8].

Motivated by the successful development of intermetallic H_2 storage materials, hydrides of light metals have been increasingly attracting attention, aiming to enhance the hydrogen storage density [10]. One of its promising playgrounds is magnesium (Mg)-based compounds, which host the merits of good capacity as high as 7.6%, satisfying the US Department of Energy (DOE) target, excellent reusability, environmental-friendly, and high Clarke number characteristics [11,12]. However, the mass-scale commercialization of Mg-based H_2 storage systems (e.g., using in fuel cell vehicles (FCVs)) has not yet been realized due to the remaining challenges. The bottle-neck is the high operation temperature and slow dehydrogenation reaction rate. As shown in Fig.1, these issues are closely associated with the thermodynamics

and kinetics of hydrogenation reactions. To be specific, during the H_2 storage cycle, the formation of strong chemical bonds between Mg and hydrogen atoms leads to high thermodynamic stability and thus the large reaction enthalpy change. For instance, the enthalpy change (ΔH) of Mg metal reaches ~ 75 kJ/mol, resulting in high operating temperature and low equilibrium pressure and ultimately hindering their further practical applications. Moreover, the lack of active sites on the Mg/MgH₂ surface gives rise to high energy barriers for dissociation/recombination and diffusion processes, resulting in low hydrogenation/de-hydrogenation rates.

To improve the thermodynamic and kinetic properties of Mg-based H_2 storage materials, various investigations have been conducted. In this review, we concentrate on the thermodynamic and kinetic fundamentals of hydriding and dehydriding reactions, and discuss the advanced methodologies employed for improving the properties of Mg-based hydrogen storage materials. In particular, the significance of nano-size effect, alloying and composite structure on improving the thermodynamic properties is elucidated. The influence of catalytic, surface treatment, and nano-sizing on kinetic performances are also discussed. Subsequently, the remaining challenges in developing novel Mg-based hydrogen storage materials are summarized. It is expected that our endeavor in this review can inspire more new ideas to expedite the development in related fields and beyond.

2. Thermodynamic properties of Mg-based hydrogen storage materials

2.1. Thermodynamic principles of the hydriding/dehydriding reaction in Mg-based hydrogen storage materials

2.1.1. The classical thermodynamics of hydriding/dehydriding reaction

In H_2 storage materials, the hydrogenation and dehydrogenation process involve the reaction between bulk materials and H_2 gas. The hydrogenation reaction of Mg-based hydrogen storage alloys can be simply expressed as



where Me represents substitutional alloying elements. The molar Gibbs free energy of the reaction can be formulated as

$$\Delta G = \Delta G^\circ + RT \ln \frac{a_{\text{Mg}_x\text{Me}_y\text{H}_2}}{a_{\text{Mg}_x\text{Me}_y} P_{\text{H}_2}^{eq}} \quad (2)$$

The activity (a) of solid hydrogen storage alloys and hydrides is approximately close to 1. At the equilibrium state ($\Delta G = 0$), the van't Hoff equation can be expressed as:

$$\ln P_{\text{H}_2}^{eq} = \frac{\Delta H^\circ}{RT} - \frac{\Delta S^\circ}{R} \quad (3)$$

where $P_{\text{H}_2}^{eq}$ is the equilibrium pressure of H_2 , ΔH° and ΔS° represent the standard enthalpy and entropy change, respectively. The equilibrium pressure of H_2 depends on the temperature, enthalpy, and entropy change of the reaction.

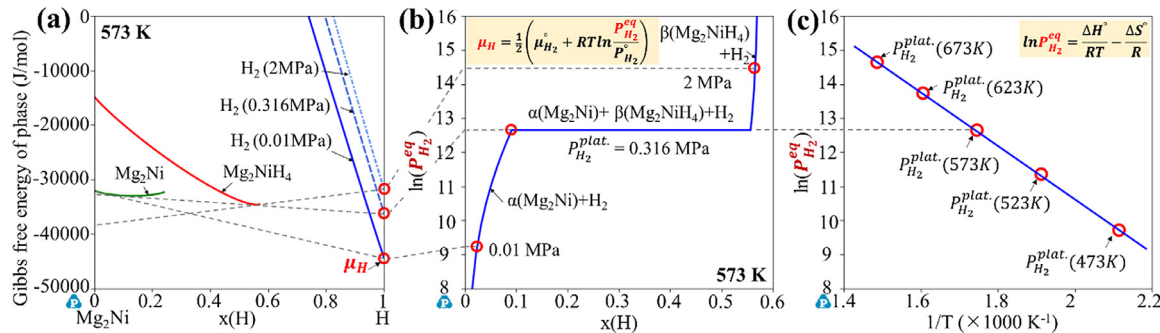


Fig. 2. Schematic diagram of the relationship between Gibbs free energy, hydrogen chemical potential, equilibrium pressure $P_{H_2}^{eq}$ and van't Hoff equation: (a) the Gibbs free energies of Mg₂Ni, Mg₂NiH₄ and hydrogen at 573 K, (b) the P-C-T curve of Mg₂Ni at 573 K, and (c) the van't Hoff relation for Mg₂Ni + 2H₂ ↔ Mg₂NiH₄ reaction.

Fig. 2 shows the correlation between Gibbs free energy, hydrogen chemical potential, the equilibrium pressure of $P_{H_2}^{eq}$ and van't Hoff equation. Taking Mg₂Ni as the example, Fig. 2a shows the Gibbs free energies of Mg₂Ni, Mg₂NiH₄, and hydrogen at 573 K. The Gibbs free energy of hydrogen is a function of hydrogen partial pressure. Only Mg₂Ni equilibrates with hydrogen when hydrogen partial pressure is lower than the plateau pressure (0.316 MPa at 573 K). This stage corresponds to the Mg₂Ni+H₂ region in Fig. 2b. The increase of hydrogen pressure will lead to the equilibrium composition of H in Mg₂Ni shifts right side, which means the solid solution of H in Mg₂Ni increases. As the hydrogen pressure rises to 0.316 MPa, a three-phase equilibrium is reached for Mg₂Ni+Mg₂NiH₄+H₂, indicating the formation of Mg₂NiH₄. With further increasing the H₂ content, the transformation of Mg₂Ni+2H₂↔Mg₂NiH₄ continues until the Mg₂Ni is exhausted which manifests the increase of hydrogen absorption content. At fixed temperature, the freedom degree of the 2D ternary system reduces to one in three equilibria. Therefore, a plateau appears in the P-C-T curve (Fig. 2b). When H₂ pressure is higher than 0.316 MPa, there is only two-phase equilibrium Mg₂NiH₄+H₂ in the system, as shown in Fig. 2a. This state corresponds to the β(Mg₂NiH₄) + H₂ in Fig. 2b. Continuing improvement of hydrogen pressure will increase both the Gibbs free energy and the chemical potential of hydrogen.

Since the equilibrium hydrogen potential is a function of hydrogen partial pressure, as shown in Fig. 2b, the P-C-T curve can be predicted by calculating the Gibbs free energies of various phases. For the plateau pressure, we can obtain a series of $P_{H_2}^{plat.}$ (the plateau pressure of P-C-T curve) at different temperatures, which shows the linear relation between $\ln(P_{H_2}^{eq})$ and $1/T$ within a certain temperature range, as shown in Fig. 2c. The relationship between $\ln(P_{H_2}^{eq})$ and $1/T$ is denoted as van't Hoff equation. Finally, for all of the phase equilibrium, P-C-T properties including plateau pressure ($P_{H_2}^{plat.}$), hydrogen storage capacity ($x_{H, max}$), reaction enthalpy (ΔH°) and entropy (ΔS°), can be calculated based on the Gibbs free energies of phases.

The enthalpy and entropy of the hydrogenation reaction can be determined using the van't Hoff equation, i.e. Eq.(3). Accordingly, $\ln(P_{H_2}^{eq})$ linearly correlates with $1/T$, where the

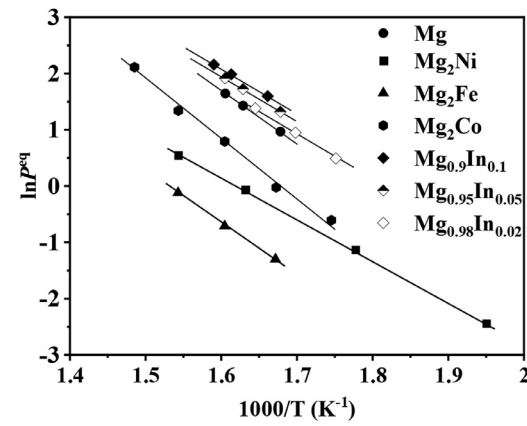


Fig. 3. van't Hoff plot of different Mg-based hydrogen storage materials at 0.1 MPa.

slope corresponds to ΔH° and the Y-intercept by extrapolating the straight line to Y-axis intersection is ΔS° . Fig. 3 shows the van't Hoff plot for typical Mg-based hydrogen storage materials at 0.1 MPa. The negative values of ΔH° indicate that the reactions are all exothermic. The larger the slope is, the greater the reaction enthalpy changes. Compared to pure Mg, the solid solution containing In slightly reduces the enthalpy, while the enthalpy of Mg₂Ni containing In reduces significantly, resulting in the decreased release temperature of H₂. The value of ΔS° is approximately equal to $-S_{H_2}^\circ$, where $S_{H_2}^\circ$ is the absolute entropy of hydrogen. The value is ca. 130.6 J/(mol·K) H₂ at 298 K, which differs slightly in different metals.

Table 1 shows the standard enthalpy and entropy of dehydrogenation reaction for several typical hydrides. Compared with Mg-based hydrides, LaNi₅H₆ in AB₅ type, TiMn₂H₃ in AB₂ type and TiFeH₂ in AB type hydrides have much lower standard enthalpy, leading to the low hydrogen release temperatures. Thus, strategies of both microstructure nanocrystallization and catalytic additive have been extensively studied to control the enthalpy change in dehydrogenation process for Mg-based hydrogen storage alloys because the relatively large reaction enthalpy of Mg-based hydrogen storage alloys leads to higher hydriding/dehydriding temperatures [13,14]. In addition, the equilibrium plateau on P-C-T curve

Table 1

Standard enthalpy and entropy change for hydrogen release in various hydrides.

Hydride	Desorption temperature (°C)	ΔH° (kJ/mol)	ΔS° (J/(mol·K))
MgH ₂	300	-74.4	130.1
Mg ₂ NiH ₄	254	-64.4	122.2
Mg ₂ FeH ₆	310	-80.0	137.0
Mg ₂ CoH ₅	317	-79.0	134.0
LaNi ₅ H ₆	10	-30.9	109.0
TiMn ₂ H ₃	-57	-24.6	114.0
TiFeH ₂	-8	-28.1	106.0

Note: The desorption temperature is given at 0.1 MPa hydrogen pressure.

of Mg-based hydrogen storage alloys is much flatter and wider than other hydrogen storage materials, implying the relatively large hydrogen storage capacities.

As mentioned above, the high hydrogen release temperature of Mg-based hydrides is a bottleneck of its applications. Various methods, including alloy addition (e.g., Ni, Cu, Al, Ti, Fe, Nb, La, Ce, Y, and Si) and controllable processing techniques (ball milling, amorphization, microwave, and magnetic treatment), have been used to improve the thermodynamic properties of hydrogen absorption and desorption. The aim of these strategies is to reduce the reaction energy difference by reducing the enthalpy through alloying, increasing the surface energy by downsizing, or introducing additional energy from the external field. In the following part, the theoretical background and the feasibility of these methods will be briefly summarized.

According to Eq.(2), the change in Gibbs free energy involving surface energy and additional energy terms can be expressed as

$$\Delta G = \Delta G^0 + RT \ln \frac{a_{Mg_xMe_yH_2}}{a_{Mg_xMe_y}P_{H_2}^{eq}} + \Delta G^{surf} + \Delta G^{ext} \quad (4)$$

where ΔG^{surf} is the surface energy difference between Mg_xMe_y and $Mg_xMe_yH_2$; ΔG^{ext} is the energy contribution from the external field. When the equilibrium state achieves, Eq.(4) can be simplified as

$$RT \ln P_{H_2}^{eq} = \Delta H^\circ - T \Delta S^\circ + \Delta G^{surf} + \Delta G^{ext} \quad (5)$$

which can be reformulated as

$$\ln P_{H_2}^{eq} = \frac{\Delta H^\circ + \Delta G^{surf} + \Delta G^{ext}}{RT} - \frac{\Delta S^\circ}{R} \quad (6)$$

Bérubé et al. [15] investigated the effect of particle size on the heat of formation for hydrides, in which the surface energy difference is expressed as

$$\Delta G^{surf} = \frac{3V_{MgMe}E(\gamma, r)}{r} \quad (7)$$

The surface energy $E(\gamma, r)$ depends on the surface energy per unit area γ and the particle radius r , which is described via the equation:

$$E(\gamma, r) = \left[\gamma_{Mg_xMe_yH_2}(r) \left(\frac{V_{Mg_xMe_yH_2}}{V_{MgMe}} \right)^{\frac{2}{3}} - \gamma_{MgMe}(r) \right] + E_{ads} \quad (8)$$

where V_{MgMe} and $V_{Mg_xMe_yH_2}$ are the molar volumes of $MgMe$ and $Mg_xMe_yH_2$, respectively. E_{ads} represents the reduction of the surface energy by bonding hydrogen on the surface of metals or hydrides. After the hydrogenation, the lattice expands and the volume of $Mg_xMe_yH_2$ ($V_{Mg_xMe_yH_2}$) usually increases by ca. 10–20% than the original volume of $MgMe$ (V_{MgMe}).

The influence of the magnetic field on the Gibbs free energy can be evaluated via

$$\Delta G^{ext} = \left(G_{Mg_xMe_yH_2}^{mag} - G_{Mg_xMe_y}^{mag} \right) - \left(E_{Mg_xMe_yH_2}^{mag} - E_{Mg_xMe_y}^{mag} \right) \quad (9)$$

where $G_{Mg_xMe_yH_2}^{mag}$ and $G_{Mg_xMe_y}^{mag}$ are the magnetic free energies of $Mg_xMe_yH_2$ and $MgMe$, respectively. They both can be described as a function of magnetic moment and Curie temperature within the Hillert-Jahl model [15]. $E_{Mg_xMe_yH_2}^{mag}$ and $E_{Mg_xMe_y}^{mag}$ are the magnetostatic energies of the two phases induced by the external magnetic field, which can be calculated by

$$E_\phi^{mag} = \int_0^B m(T, B) dB \quad (10)$$

where $m(T, B)$ is the magnetic susceptibility that depends on temperature and the magnetic field.

As shown in Eq.(6), all of the standard enthalpy change, surface energy, and magnetic free energy have an impact on the heat of reaction and the equilibrium pressure. The standard enthalpy depends primarily on the chemical potential and hence changes with alloy composition. Furthermore, reducing the size of MgH₂ or introducing an external field can reduce the enthalpy change.

2.1.2. The quantum statistical mechanics of hydriding/dehydriding reaction

Self-consistent electronic structure calculations within the density functional theory (DFT) is powerful method used for hydrogen storage simulations [16–20]. It can predict energetics and structures, benefitting to design novel hydrogen storage materials based on the fundamental understanding of atomic mechanisms [21]. In DFT calculations, the motion of electrons within the fully interacting system is mapped onto a fictitious state that electrons experience an effective potential within a non-interacting system. The electron density minimizing the total energy and describing the ground-state properties can be determined by solving self-consistently the one-electron Kohn-Sham equations [22,23].

The binding strength of hydrogen is the most important factor for H₂ storage materials because it associates with enthalpy of formation and plateau pressure, and the kinetics of hydrogen release procedure [24]. The strength of hydrogen bonds can be evaluated by the following equation:

$$E(H) = \frac{1}{N} \left[E_t(X - NH) + \frac{N}{2} E_t(H_2) - E_t(X) \right] \quad (11)$$

where $E(H)$ is the binding energy of hydrogen (or equivalent to the absorption energy); $E_t(X)$ and $E_t(X - NH)$ represent the total energy of the original system and the total energy of

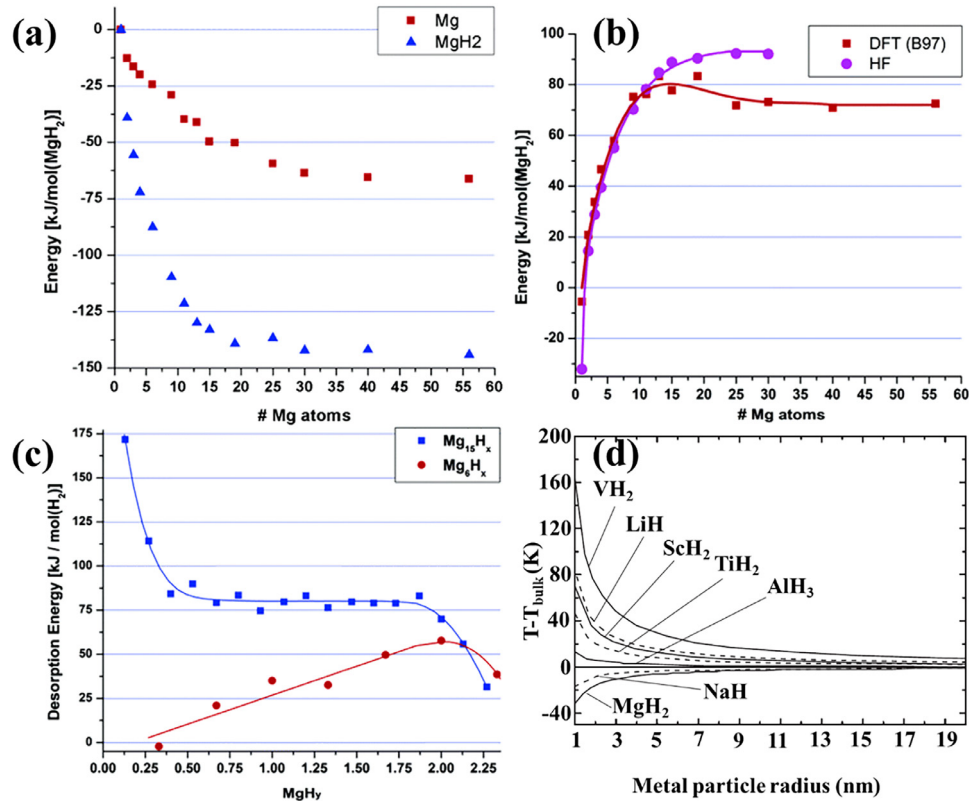


Fig. 4. (a) The calculated energy and (b) energy difference of Mg and MgH₂ clusters as a function of Mg atoms included. (c) The H₂ desorption energy of Mg₆H_x (red line) and Mg₁₅H_x (blue line) as a function of normalized hydrogen content. (d) The difference of metal/metal hydride reaction enthalpy as a function of particle sizes. The figures are reproduced with permission from Refs. [25] and [27].

the hydrogen deficient system, respectively. $E_t(\text{H}_2)$ is the total energy of a H₂ molecule in vacuum. The value of $E(\text{H})$ represents the binding energies of hydrogen atoms with the host materials. For hydrogen storage applications, binding energy ranging from 0.1 eV/H to 0.35 eV/H are considered suitable [21].

Mass-scale applications of Mg-based hydrogen storage materials are currently hindered by the strong thermodynamic stability and Mg-H bonding. How to weak these chemical bonds? One option is nano-crystallization. Wagemans et al. investigated the size effect of the Mg and MgH₂ clusters using DFT calculations [25]. Their results show that the lattice energies remain unchanged when the clusters are composed of 19 Mg atoms and more, as shown in Fig. 4a. However, the cluster energies of both Mg and MgH₂ increase with further decreasing cluster size. The lattice energy modification of MgH₂ is more significant than that of Mg, resulting in the relatively smaller hydrogen desorption energy gap of the Mg/MgH₂ system (Fig. 4b). The desorption temperature and enthalpy were estimated to be ~200 °C and 63 kJ/mol for Mg₉H₁₈, in which the cluster size corresponds to ~0.9 nm [25]. With further downsizing the cluster toward the smallest unit, the hydrogen desorption enthalpy even may go negative, i.e., Mg₂H₄ is energetically unstable relative to the Mg cluster. Similar conclusions were reached by Cheung et al. [26] using Reactive Force Field simulations. In addition, the

nano-size effect is also expected to boost hydrogen desorption with the hydrogen-poor condition. For example, when the Mg/H ratio becomes lower than 0.5, the hydrogen desorption energy increases for the 15 Mg atom cluster model (Mg₁₅H_x) but decreases for the 6 Mg atom cluster model (Mg₆H_x), as shown in Fig. 4c [25].

Although the nano-crystallization is helpful to improve thermodynamic properties in the Mg/MgH₂ systems, it cannot be applied to a wide range of materials. For example, Kim et al. [27] systematically investigated the impact of nano-crystallization of seven metals (Mg, Li, Na, Sc, Ti, Al, and V) and their hydrides. The results show that the energy gap of hydrogen desorption could be suppressed with downsizing particle size for MgH₂ and NaH, while increases for the other systems, LiH, ScH₂, TiH₂, and AlH₃ (Fig. 4d). The root-cause of the nano-size effect on thermodynamic properties is the energies of hydrides relative to corresponding metals, since the free energies of both metal and hydride increase with downsizing particle size. Because nanoparticles exhibit a much larger surface area than the corresponding bulk materials, their surface energy depends on crystal morphology and exposed planes.

One of the highlighted advantages of DFT is that various calculations can be conducted based on any structural models [28]. Wagemans et al. reported the modifications of thermodynamic properties of Mg/MgH₂ with different particle sizes,

and found that the system becomes more thermally unstable with decreasing particle sizes. Obviously, it is difficult to precisely control the particle size in experiments, showing the importance of DFT methods on investigating the H₂ storage materials. Moreover, DFT calculation provides a promising platform to unveil the dynamics of hydrogenation process, offsetting the deficiency of experimental methods, since the existing experimental technique is difficult to observe the hydrogen species. It enables the analysis of hydrogenation process of specific surface, e.g. Mg (0001) plane, giving an important insight for further material design. Meanwhile, the DFT calculation, particularly for slab models, typically needs larger input models than bulk materials and thus consumes more computer resources. Furthermore, implementing strong correlation and spin-polarization 3d transition metals is still challenging, which should be addressed in the future studies.

2.2. Improvements on the thermodynamic properties of magnesium-based alloy

2.2.1. The effect of alloying elements

The addition of alloying elements is a standard method to improve alloys' properties. The alloying technique can be divided into two types, doping and substitution. Doping means adding trace of alloying elements, while substitution is using substantial amounts of elements to substitute the atoms in major structure. Both methods modify the hydriding/dehydriding thermodynamic properties of magnesium-based alloys.

The major issue of the Mg is its high hydrogenation and dehydrogenation enthalpies, resulting in high desorption temperature (>300 °C) of MgH₂ at 0.1 MPa. The doping of transition elements (Ni, Ti, Fe, etc.) and/or other representative elements (N, B, etc. [29,30]) shows a significant improvement in desorption behavior. Bis(cyclopentadienyl) nickel II is a good precursor of nickel catalyst which decomposes into metallic nickel during ball milling process with MgH₂ and homogeneously dopes over the Mg-MgH₂ surface [31]. The catalyzed MgH₂ desorbs hydrogen below 225 °C under Ar flow and absorbs hydrogen at 50 °C under 1.5 MPa H₂. The Fe-doped Mg could be hydrogenated at 0 °C up to 45% of the theoretical hydrogen storage capacity within an hour and the dehydrogenation started below 150 °C, which is attributed to the nano-engineered surface of MgH₂ by Fe [32]. The interstitial doping of nonmetallic elements is another effective way to improve the hydrogen storage properties of Mg-based metal hydride. Wu et al. [33] used first-principle calculations to investigate the influences of N concentration on the hydrogen absorption/desorption thermodynamics of the Mg₂NiN_x system. It was found that the formation enthalpy and dehydrogenation energy of Mg₂NiN_{0.5} reduce by 98% and 59%, respectively, due to the strong hybridization between the orbits of N and H.

Elemental substitution is an effective method for improving the H₂ storage properties of pure Mg and Mg-based intermetallics. At the expense of moderate capacity, its thermodynamic properties can be optimized by modulating the structure and composition of Mg [34]. Mg(In) solid solution

absorbs H₂ to form MgH₂ and a disordered MgIn compound [35], where the Mg_{0.95}In_{0.05} solid solution shows reduced hydrogen sorption reaction enthalpy of 68.1 ± 0.2 kJ/mol. In addition, considering the high cost of In, various of investigations were carried out to improve the hydrogen storage properties of Mg using more affordable elements instead of In. For example, Al can dissolve into MgIn compound to form Mg-In-Al ternary system [36]. Mg_{0.9}In_{0.05}Al_{0.05} has a reversible capacity of 5.0 wt.% which is slightly higher than that of Mg_{0.9}In_{0.1} alloy. The desorption enthalpy ΔH of Mg_{0.9}In_{0.05}Al_{0.05} is determined to be 66.3 kJ/mol, showing that the Al addition further decreases the ΔH of Mg(In) solid solution. Mao et al. [37] proposed a new strategy to improve the thermodynamic properties of MgH₂ using the structural transformation from a solid-solution to a core-shell structure during de/hydrogenation process. The Mg-In and Mg-Ag alloys transform to MgH₂@MgIn and MgH₂@MgAg core-shell structure by self-assembly during the hydrogenation process, and change back to Mg-In and Mg-Ag solid solutions by reversible organization after dehydrogenation through a diffusion-controlled two-step reaction.

Although the thermodynamic properties of Mg₂NiN_x and Mg-(Al, In, Ag) were better than MgH₂ system [38], it is still far from the requirement of practical applications. The substitution of third element on Mg or Ni sites was therefore investigated to lower thermodynamic stability of the Mg₂Ni compound. IA~VB group elements (Ti, V, Zr, Ca and RE) can substitute the Mg site, while VI B~VIII B group elements (Mn, Fe, Co, Cr, Cu and Ag) can replace Ni [39–42]. Takahashi et al. [43] calculated the electronic structure of the 3d transition metal TM (TM = V, Cr, Fe, Co, Cu, Zn) alloyed Mg₂NiH₆ cluster using the DV-X α method based on the molecular orbital theory. When different TM replaced Ni sites, the weaker bond formation between TM-Mg decreases the structural stability of Mg₂Ni hydride. The replacement of Ni in Mg₂Ni by Cr, Mn and Co lowers the decomposition plateau pressure, Ti and Cu demonstrate the opposite effects, while the influence of Fe and Zn can be neglected [44].

2.2.2. Composite Mg based materials

The construction of Mg-based composite is an approach to achieve thermodynamic destabilization by changing the reaction path of the hydrogenation/de-hydrogenation [45,46]. Using additives that can react with metal hydrides makes it possible to generate hydrogen with different chemical reaction paths. The additives can be classified into three categories according to their effects: active hydrogenates, reversible intermetallics and ligand hydrides.

The active hydrogenates may promote the hydrogenation/dehydrogenation process of Mg/MgH₂, which includes REH₂, TiH₂, etc. The rare-earth elements, such as Y, La, Ce, Pr and Nd, can form a series of intermetallic compounds with Mg, such as REM₁₂, RE₂Mg₁₇, RE₅Mg₄₁, REM₃, REM₂, REMg, etc. Due to the affinity of RE elements and hydrogen, those RE-Mg intermetallics decompose into REH₂₋₃ and MgH₂ during the hydrogenation, among which REH₂₋₃ is stable in the following hydriding/dehydriding cycles. The en-

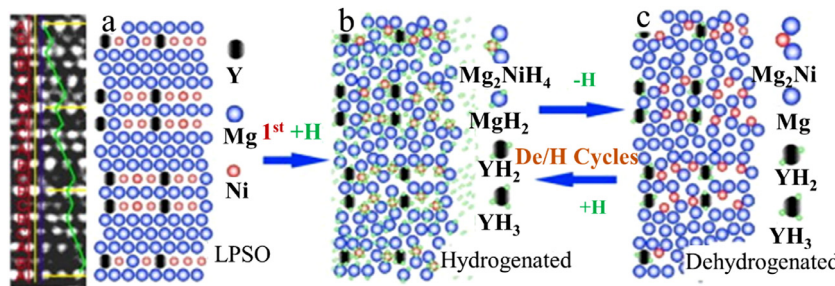


Fig. 5. The microstructural mechanism and the evolutions of 18R-LPSO structure during the hydrogenation and dehydrogenation [55].

thalpy and entropy of $\text{RE}\text{Mg}_3\text{-H}$ dehydriding reaction were determined to be 81.0 kJ/mol and 142 J/(mol·K) from P-C-T curves [47].

The further addition of transition metal elements is common to form the composite of $\text{REH}_2\text{-Mg-Mg}_2\text{Ni}$ which exhibits great kinetic properties, while it plays a little contribution to thermodynamic improvement [48–54]. Fig. 5 shows the microstructural mechanism and evolution of Mg-NiY 18R-LPSO structure during the hydrogenation and dehydrogenation [55]. The desorption enthalpy of MgH_2 was 74.5 kJ/mol for $\text{Mg}_{90}\text{Ce}_5\text{Ni}_5$ alloy [56] and 79.1 kJ/mol for $\text{Nd}_4\text{Mg}_{80}\text{Ni}_8$ alloy [57]. Ouyang et al. [58] reported that $\text{CeH}_{2.73}\text{-MgH}_2\text{-Ni}$ nanocomposites in-situ formed from the hydrogenation of as-melt $\text{Mg}_{80}\text{Ce}_{18}\text{Ni}_{12}$ alloy show good cycling stability where the desorption enthalpy and entropy are almost unchanged even up to 500 cycles. The in-situ hydrogenation of single intermetallic compounds of $\text{Nd}_4\text{Mg}_{80}\text{Ni}_8$ and 18R-LPSO leads to form nanocomposites of $\text{NdH}_2\text{-MgH}_2\text{-Mg}_2\text{NiH}_4$ and $\text{YH}_2\text{-MgH}_2\text{-Mg}_2\text{NiH}_4$ [59–61]. The composite of $\text{NdH}_2\text{-MgH}_2\text{-Mg}_2\text{NiH}_4$ achieves superior stability of 819 cycles with 80% hydrogen storage capacity remains.

LaNi_5 compound in the Mg-LaNi_5 nanocomposite decomposes upon hydrogenation, transforming to a new composite of $\text{MgH}_2\text{+LaH}_3\text{+Mg}_2\text{NiH}_4$. The monoclinic Mg_2NiH_4 phase is obtained when hydriding at low temperature, while the orthorhombic Mg_2NiH_4 structure is formed at higher hydrogenation temperatures (above 523 K) [62]. The $\text{MgH}_2\text{+LaH}_3\text{+Mg}_2\text{NiH}_4$ composite exhibits great improvement on kinetic performance and thermodynamic properties. The Mg-30 wt.% LaNi_5 alloy could be obtained by hydriding combustion synthesis followed by mechanical milling, and the optimized enthalpies were 77.19 kJ/mol for Mg and 59.61 kJ/mol for Mg_2Ni in Mg-30 wt.% LaNi_5 composite according to the van't Hoff equation [63]. The Mg-5 wt.% LaNi_5 nanocomposite was prepared by mixing Mg (200 nm) and LaNi_5 (25 nm) nanoparticles ultrasonically, and the decomposition enthalpy was reported to be ca. -76.0 kJ/mol. This indicates that the addition of LaNi_5 nanoparticles does not apparently alter the thermodynamics of MgH_2 due to the low content of 5 wt.% [64].

Ligand hydrides were added into Mg based systems to improve the hydrogen storage capacity of the composites. Here ligand hydrides indicate the hydrides formed by representative elements, such as Al, B, N, that form covalent bonds with

hydrogen together with ionic bonds with metals. They can be classified into three categories according to the element difference: the first is metal-aluminum (Al) hydrides containing $[\text{AlH}_4]$ -ligands, such as LiAlH_4 , NaAlH_4 , and $\text{Mg}(\text{AlH}_4)_2$, etc. [65–68]; the second is metal-boron (B) hydrides containing $[\text{BH}_4]$ -ligands, such as LiBH_4 , NaBH_4 , and $\text{Mg}(\text{BH}_4)_2$, etc. [69,70], and the third is metal-nitrogen (N) hydrides containing $[\text{NH}_2]$ -ligands, such as LiNH_2 and $\text{Mg}(\text{NH}_2)_2$ [71,72]. Compared to the conventional metal hydrides, those ligand hydrides have much higher hydrogen density. However, the ionic and covalent bonds also give rise to the high thermodynamic stability. Meanwhile, the MgH_2 -ligand hydride composite systems can change the reaction path of the hydrogen generation reaction by forming intermetallic compounds, which reduces the thermodynamic stability of the reaction systems while maintaining a high hydrogen storage capacity.

The composite $\text{LiBH}_4\text{-MgH}_2$ with the presence of 2–3 mol% TiCl_3 reduced the overall reaction enthalpy by 25 kJ/mol compared with pure LiBH_4 [73]. Small amount of LiCl is also confirmed plausibly due to the reaction between TiCl_3 and LiBH_4 . LiCl and MgB_2 are confirmed as main phases after dehydrogenation at 450 °C. The composite undergoes a re-hydrogenation process at 350 °C and under 100 bar, re-forming LiBH_4 and MgH_2 phases again, while LiCl phase disappears. The overall reaction is summarized in the Eq. (12). The reaction enthalpy is estimated to be 40.5 kJ/mol, which is smaller than the de-hydrogenation process of both MgH_2 and LiBH_4 .



2.2.3. Nano-crystallization

As discussed in the previous sections, nano-crystallization is one of the promising techniques to improve the thermodynamics of H_2 storage materials. In this section, the ball-milling, gas-phase reactions and chemical reduction techniques to prepare nanoparticles as well as their impact on thermodynamics of Mg-based materials are discussed in detail.

In Mg metal, downsizing particles is predicted as a practical approach to improve its thermodynamic properties. Thus, various methods were attempted to synthesize nanoparticles (NPs) of Mg/ MgH_2 . Amongst these, ball-milling is a traditional but effective technique on suppressing particle diameter. Since Mg metal and many Mg-based alloys are sen-

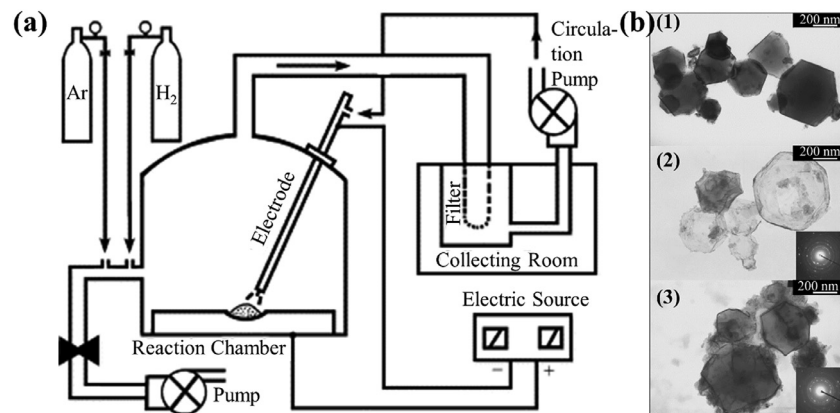


Fig. 6. (a) The schematic illustration of Ar/H₂ arc-evaporation technique. (b) The TEM observations of obtained Mg NPs. The figures are reproduced from Ref. [75].

sitive to air and moisture, ball-milling offers a low-cost and inert environment for sample preparation. Varin et al. [74] prepared MgH₂ fine powders using ball-milling with various parameters, such as milling time, rotation speed, etc. SEM images show that the minimum particle size of MgH₂ is ca. 600 nm which is obtained under the optimized ball-milling condition (175 rpm for 100 h). Accordingly, the H₂ desorption temperature decreases from 414 °C to 360 °C.

However, despite of decades of unremitting efforts, critical issues of ball-milling are remaining unsolved. First, reducing particle size below 500 nm is still challenging, and the homogeneity of particle size cannot be well controlled. Second, ball-milling easily damages both surface and bulk structure of materials, resulting in low crystallinity and even amorphous structure. Third, Ball-milling should not be considered an option for material synthesis if a function is derived from their specific surface/bulk structure. The surface damage may even increase their surface energy by introducing defects and disordering, making the materials more sensitive to air and moisture. Finally, due to the high surface energy, the ball-milled sample tends to aggregate to reduce the surface energy for reaching a more stable state.

To obtain NPs with better crystallinity and clearer surface structure, the gas-phase reaction method is proposed as one option. How metallic elements be evaporated into the gas-phase state? One of the solutions is using high-temperature plasma treatment under Ar, H₂, or Ar/H₂ atmosphere [76]. This technique was proven effective for preparing varieties of elemental metallic NPs. Even NPs with strong oxygen affinities, such as Ti, Sc, V, and Ta, were obtained by this method and have a particle size of ~200 nm [76]. Subsequently, Shao et al. applied this technique to Mg, and obtained Mg NPs with the particle size of 200–500 nm [75]. The Mg particle can be further suppressed using Ar/C₂H₂ plasma instead of Ar/H₂ plasma [77]. The particle size of Mg NPs decreases with increasing C₂H₂ partial pressure and the mean particle size is only ~40 nm which is obtained under the optimized reaction condition (C₂H₂: 21.7–28 mol%). The mechanism is that more C₂H₂ decompose to C with increasing C₂H₂ ratio,

and Mg NP size was limited by the deposited carbon on Mg surface by hindering the crystal growth.

Despite much progresses were made by the high-temperature plasma treatment, many issues remain. The first one is associated with the synthesis condition. Because each element has different vapor pressure, the optimization of vapor pressure is essential to obtain desired phases if the target contains several elements. Second, the device structure leads to a low yield issue. Fig. 6a shows that the evaporated metal transfers from the reaction chamber to the sample collecting room. During this process, a fair amount of metal gas is also absorbed on the wall of the equipment, resulting in a low yield of NPs. Last, this technique is not suitable for mass production, and difficult to produce kg scale of NPs due to the high cost and low efficiency [78].

Comparatively, chemical reduction methods appear to be a more economical and practical approach. One of the successful examples is the synthesis of Mg nano-crystals using metal-organic compounds, such as magnesocene (MgCp₂), as starting Mg sources. Norberg et al. [79] reported that MgCp₂ could be reduced to Mg nano-crystals using strong reducing agents, e.g., potassium biphenyl, potassium phenanthrene, and potassium naphthalin, etc. The synthesized Mg crystals are in the size of ~30 nm, one order of magnitude smaller than those by previously reported ball-mill (top-down) techniques (Fig. 7). Subsequent studies further optimized the reducing agents and Mg sources. The particle size could be further suppressed to 10–40 nm using Mg(n-Bu)₂ as Mg source and optimized solvents [80,81]. By reducing the particle size of Mg/MgH₂, the reaction enthalpy was reduced to 63.5 kJ/mol for the optimized condition (8–34 nm). At the same time, the hydrogen desorption temperature was decreased to ~335 °C [80,81].

The nano-crystallization can enhance the thermodynamics of hydrogen storage process without sacrificing hydrogen capacity. However, two more challenging issues need to be addressed. For one thing, the synthesized NPs are sensitive to thermal energy. The particle size increases from 27 nm to 90 nm after applying temperature of 300–375 °C, lacking recycle stability [78]. It should be noted that particle aggre-

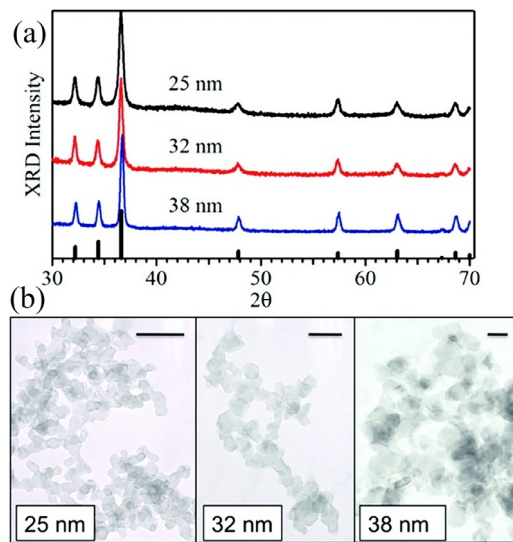


Fig. 7. (a) The powder XRD and (b) TEM observations of synthesized Mg nano-crystals. The figures are reproduced from Ref. [79].

gation is a universal issue due to its relatively high surface energies [82]. For the other, it is still challenging to prepare NPs with particle sizes smaller than 10 nm. Given that the nano-size effect becomes significant at the sub-nm scale, the improvement of intrinsic thermal dynamics is not substantial, further downsizing particle size is required. In the future studies, the combination of chemical reduction method and attaching NPs on appropriate supports are becoming increasingly important to further suppress the particle size and avoid particle aggregation.

3. Kinetic performances of Mg-based hydrogen storage materials

3.1. Kinetic models and analysis methods on the hydriding/dehydriding reaction

As shown in Fig. 8, the hydrogen absorption process on Mg-based materials is suggested to occur via the following steps at the mesoscopic scale: (1) H₂ transport to and physisorption on the surface. The physisorption process refers to H₂ being adsorbed on the Mg-based metals' surface through intermolecular forces or Mg-H bonds formation; (2) chemisorption and dissociation of H₂ on the surface of Mg-based materials; (3) penetration and diffusion of the H₂ into the Mg-based materials (α phase); and (4) nucleation and growth of Mg hydride (β phase) in the H₂ supersaturated region [83–87]. Accordingly, the hydrogen release process is regarded as their inverse processes. The rate-determining step may vary for different Mg-based hydrogen storage materials.

The hydrogen storage/release process is a typical gas-solid multi-phase reaction, where different energy barriers at each stage should be considered. During the hydrogenation process, the kinetics may degrade because of the following issues: (1) MgH₂ can form on the surface of bulk Mg and prevent the hydrogen diffusion on the Mg surface. For example, the hy-

drogen diffusion rate on MgH₂ ($1.5 \times 10^{-16} \text{ m}^2/\text{s}$, 300–600 K) is much lower than that on Mg ($4 \times 10^{-13} \text{ m}^2/\text{s}$, 493–473 K). (2) The formation of Mg metal on MgH₂ surface is thermodynamically unfavored. (3) The hydrogen dissociation/recombination on Mg surface typically needs to overcome high activation barriers. It worsens if impurity phases, such as MgO and Mg(OH)₂, are formed on Mg surface. Therefore, in order to improve the kinetics of hydrogen storage/release in Mg alloys, it is required to optimize the hydrogen dissociation and diffusion routes on surface.

First of all, the classical kinetic process of incompressible flow and physisorption needs to be considered for H₂ physisorption on Mg surface. The transport process of H₂ gas to the surface of the Mg-based metal is mainly driven by pressure differences. From the macroscopic perspective, the hydrogen absorption/desorption rate, the shape of the hydrogen storage materials and the container will affect the flow distribution. The gas-surface interaction between H₂ and hydrogen storage materials occurs in the boundary layer on the mesoscopic scale. A “local equilibrium” is reached between H₂ transportation and adsorption onto the surface of storage materials. The adsorption process can be described by the extension of Langmuir theory, in which the monolayer adsorption is first formed on the storage materials. After the monolayer adsorption saturates, the multi-layer adsorption randomly occurs on the first layer. The uppermost molecule layer is always in equilibrium with the gas phase H₂. From a dynamic point of view for ad-/de-sorption, the reaction rate of this process can generally be described by the following equation:

$$v_{ph} = k_{ab}^{ph}(1 - \theta_{ph})P - k_{de}^{ph}\theta_{ph} \quad (13)$$

where k_{ab}^{ph} and k_{de}^{ph} are the kinetic coefficients of physical ad-/de-sorption, respectively, which depends on temperature and activation energy based on the Arrhenius formula. θ_{ph} is the surface coverage ratio, and P is the hydrogen gas pressure.

According to the Arrhenius formula, Eq.(13) can also be expressed as,

$$v_{ph} = k_{ab,0}^{ph} \exp\left(-\frac{E_{ab}^{ph}}{RT}\right)(1 - \theta_{ph})P - k_{de,0}^{ph} \exp\left(-\frac{E_{de}^{ph}}{RT}\right)\theta_{ph} \quad (14)$$

where E_{ab}^{ph} and E_{de}^{ph} are the activation energies of ad-/desorption, respectively, T is temperature (K), and R is the gas constant.

If the physical adsorption does not require activation energy and the adsorption rate in the process is much faster than the desorption rate, Eq. (14) can be expressed as,

$$v_{ph} = k_{ab,0}^{ph}(1 - \theta_{ph})P \quad (15)$$

For the second step in Fig. 8, the chemisorption and dissociation of hydrogen occur on the surface of the Mg-based materials. The dissociation of hydrogen can be expressed as $H_2 \rightleftharpoons 2[H]$, and H₂ is transformed into hydrogen atoms that can diffuse into metals and hydrides. Chemisorption is the kinetic process, in which the H₂ molecules coordinate with the

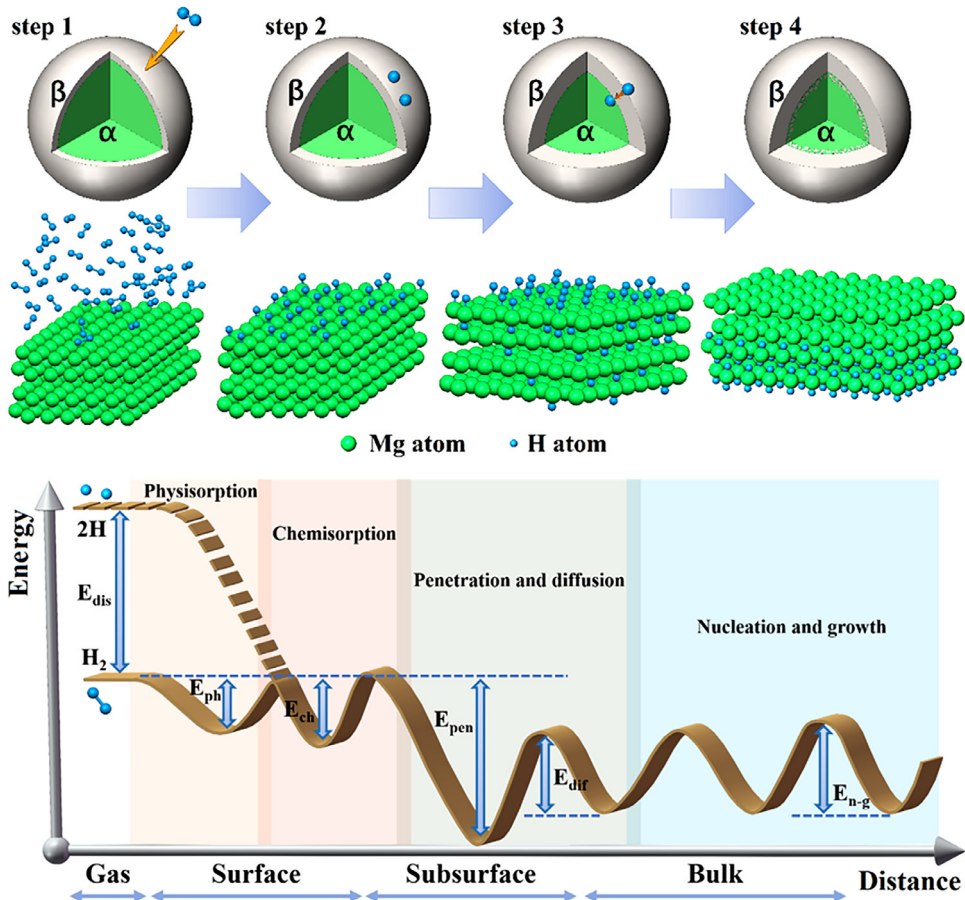


Fig. 8. Schematic illustration of the kinetic steps in hydrogen storage process (up) and Lennard-Jones potential diagram [88] describing continuous energy barriers in the process of hydrogen absorption and desorption (down).

exposed alloy surface. This process involves electron transfer, atomic rearrangement, and chemical bonds dissociation and formation. The defects, edges, steps, grain boundaries, and other impurities can facilitate the chemisorption as active sites. After H₂ absorption, the H₂ molecule decomposes into two hydrogen ad-atoms, occupying the active sites. Once H atoms fully cover exposed active sites, the chemisorption process on the surface is saturated. Generally, the kinetic rate of chemisorption can be calculated by the Elovich equation, which can be expressed as,

$$v_{ch} = k_{ab,0}^{ch} \exp\left(-\frac{E_{ab}^{ch} + a\theta_{ch}}{RT}\right)(1 - \theta_{ch})^2 P + k_{de,0}^{ch} \exp\left(-\frac{E_{de}^{ch} + b\theta_{ch}}{RT}\right)\theta_{ch}^2 \quad (16)$$

where a and b are coefficients related to the surface state of the particles, and θ_{ch} is between 0 and 1. A lower θ_{ch} value represents a smaller reverse rate of chemisorption. When the last term of Eq. (16) approaches to 0, the kinetic equation of chemisorption can be simplified as,

$$v_{ch} = k_{ab,0}^{ch} \exp\left(-\frac{E_{ab}^{ch} + a\theta_{ch}}{RT}\right)P \quad (17)$$

When the value of θ_{ch} is medium, the influence of $(1 - \theta_{ch})^2$ and θ_{ch}^2 in Eq. (16) is too small. Therefore, the first term and second term of the right side of Eq. (16) can be merged into the kinetic coefficients $k_{ab,0}^{ch}$ and $k_{de,0}^{ch}$, which can be written as,

$$v_{ch} = k_{ab,0}^{ch} \exp\left(-\frac{E_{ab}^{ch} + a\theta_{ch}}{RT}\right)P + k_{de,0}^{ch} \exp\left(-\frac{E_{de}^{ch} + b\theta_{ch}}{RT}\right) \quad (18)$$

The third step in Fig. 8 represents penetration and diffusion of the hydrogen into the Mg-based materials. Prior to the H₂ storage, the surface of the Mg-based hydrogen storage material is covered by an oxide passivation layer [89,90]. The H₂ needs to penetrate into the passivation layer as an etchant to remove the oxide layer. However, the small diffusion coefficient of H atom in the passivation layer suppresses the hydrogen transport. Therefore, the etching of the oxide layer is the key issue to the incubation period of hydride growth. In certain locations without passivation layer, the transportation of H₂ to the metal is much faster. Then, the high concentration of hydrogen in this region is created, favoring the nucleation and growth of hydrides. In addition, the local volume expansion caused by the growth of hydride under the passivation

layer may induce microscopic cracks in the brittle passivation layer, providing a faster channel for hydrogen transport.

When the passivation layer is removed, the adsorbed hydrogen on the metal surface is directly contact with the β phase, causing hydrogen penetration. The surface penetration process refers to the chemically adsorbed hydrogen atoms on the surface passing through several atomic layers inside the alloy. Only hydrogen atoms with high energy can penetrate into the alloy. The concentration of hydrogen atoms participating in surface penetration can be calculated by $C_{sur} = k_1 \theta_{ch}$. Therefore, the kinetic rate expression of surface penetration is

$$v_{sp} = k_{ab}^{sp} C_{sur} - k_{de}^{sp} C_\beta \quad (19)$$

where k_{ab}^{sp} and k_{de}^{sp} are the kinetic coefficients, and C_β is the concentration of hydrogen in β phase.

Once the hydrogen atoms penetrate into the inside of β phase, the transport in β phase follows the classical law of diffusion, including the diffusion from the surface of the β phase to $\alpha\text{-}\beta$ phase interface, and the following diffusion from the $\alpha\text{-}\beta$ phase interface to β phase distributed in the α phase. The kinetic equation of diffusion can be expressed as,

$$\frac{\partial C}{\partial t} = \nabla \cdot (D \nabla \mu) \quad (20)$$

where C is the hydrogen concentration, D is the diffusion coefficient, and μ is the diffusion potential.

The aforementioned diffusion of the hydrogen in the solid phase can be classified into several steps, i.e., the diffusion in α phase and β phase, the redistribution at the different phase interfaces, as well as the diffusion at grain boundaries. Therefore, the diffusion coefficient (D) in Eq. (20) associates with many factors, including local temperature, phase composition, and grain boundaries/bulk regions. The expression of diffusion potential μ varies in different phases. Given that the influential factors are variable during H_2 ab-/de-sorption processes, different kinetic models are needed for each diffusion step. In the following section, the kinetic models will be introduced in detail.

Assuming that the hydrogen diffusion in β phase is the rate-determining step under constant temperature and pressure, various analytical models are derived from the diffusion equation, including the Jander model [91,92], Ginstling-Brounshtein (G-B) model [93], Valenssi-Carter (V-C) model [94] and Chou model [95–97]. These kinetic models are geometrical contraction models, which assume that the ab-/de-sorption of H_2 occurs uniformly on the surface. However, the geometrical disorder, surface roughness and heterogeneity explicitly, etc. are not taken into account. [98–100].

For the fourth step in Fig 8, the nucleation and growth of the β phase are the committed steps in hydrogen storage. These steps are realized by the generation and migration of the interface between α phase and β phase [101–106]. With the β phase grows, the hydrogen reaches the $\alpha\text{-}\beta$ interface by diffusion to participate in the chemical reaction of $Mg_xMe_y + 2[H] \rightarrow Mg_xMe_yH_2$. Furthermore, this process can be regarded as the precipitation of hydride in the supersaturated region [107]. Generally, the generation and migration

of the $\alpha\text{-}\beta$ interface are mainly affected by three factors: the local chemical driving force, the microelastic stress caused by volume expansion, and the local Laplace pressure. Based on the Stefan theory [108], the kinetic equation of the $\alpha\text{-}\beta$ interface can be expressed as,

$$v_\perp = \beta(T)(-\Delta G_{\alpha \rightarrow \beta}^{ch} - f^{ela} - \sigma \kappa) \quad (21)$$

where v_\perp is the vertical movement velocity of the interface, $\beta(T)$ is the temperature-related kinetic coefficient, $\Delta G_{\alpha \rightarrow \beta}^{ch}$ is the driving force of phase transition ($\alpha \rightarrow \beta$), f^{ela} is the microelastic stress at the interface, σ is the interface energy, and κ is the local interface curvature.

The chemical driving force $\Delta G_{\alpha \rightarrow \beta}^{ch}$ is determined by the local temperature, local concentration of hydrogen and composition of Mg-based materials. Because hydrogen preferentially diffuses along the grain boundaries in the metal, the hydrogen concentration near the grain boundary tends to be higher than that in bulk, resulting in higher chemical driving force. In addition, the kinetic factor of transformation at grain boundary is more significant than that of bulk, leading to the fast growth of hydride near the grain boundary. Therefore, the β phase tends to nucleate at the α phase grain boundary and grow towards the bulk. Second, the microelastic stress f^{ela} caused by volume expansion is the local stress distributed around the β phase [109]. Compared with the α phase, the volume of the β phase increases by ca. 20%. However, the caused stress negatively affects against the expansion phenomenon itself. Therefore, the above factors inhibit the growth of the β phase during the hydrogen storage process but promote the development of the α phase during the hydrogen release process. In the case of isothermal equilibrium, the plateau interval of hydrogen absorption/dissociation pressure is associated with the effect of the microelastic stress. In addition, the expansion caused by the precipitation of hydrides may lead to the generation of micro-cracks [110], thereby forming new gas-phase channels for hydrogen penetration. Third, the Laplace pressure $\sigma \kappa$ depends on $\alpha\text{-}\beta$ interface energy and local interface curvature, which is also the origin of Gibbs-Thomson effect. The influence of Laplace pressure is non-negligible during the β phase nucleation and initial growth stage, considering the large interface curvature.

Furthermore, some analytical models were established to describe the nucleation and growth of β phase, such as the classical JMAK model [111] and the nucleation index incorporated JMAK (NI-JMAK) model [112]. The former is suitable for isothermal conditions, while the latter that takes the effect of the self-catalysis of the nucleation into account is suitable for non-isothermal conditions. These models divide the determinants of the kinetic process into several kinetic factors [113–117], such as rate constant, activation energy, etc. It is helpful for the understanding the relationship of the volume fraction of β phase vs. time and clarifying the roles of various kinetic factors step by step.

Although there are many kinetic models of hydrogen storage/release reactions, most of them are based on three factors of kinetics: rate constant, activation energy and the corresponding kinetic equation describing the rate-determining

step. According to the analytical solutions of classical kinetic models, the experimental data of the hydrogen absorption and desorption reactions can be used to fit the rate constants. These data can be obtained from the Sievert method [100] or the flowing volumetric method [118]. For the Sievert method, the experimental data of the reaction fraction vs. reaction time and the reaction fraction change rate vs. reaction time can be used to analyze the kinetic mechanism. The flowing volumetric method is based on the experimental data of hydrogen gas pressure and time. The premise of applying this kinetic analysis method is the equilibrium pressure equation, which can be determined from the experimental P-C-T curves. When H_2 pressure is lower than or close to the equilibrium pressure of the metal hydride, the β phase cannot form and the limiting step is regarded as chemisorption or surface penetration process. When H_2 pressure is higher than the equilibrium pressure, the β phase can be readily obtained and the rate-controlling step can be considered as the diffusion of hydrogen, the nucleation, and growth of β phase. To the end, the controlling step under different pressures can be obtained according to the fitting results of the pressure-time curve.

3.2. Strategies for improving kinetics of magnesium-based alloy

3.2.1. Nano-crystallization

The nano-crystallization method does not only improve the thermodynamic properties of Mg-based hydrogen storage materials but also optimize their kinetic performances. Because the nanocrystalline structure is beneficial for shortening the diffusion distance of hydrogen, more grain boundaries provide the diffusion channels for hydrogen. Besides, the formation energy barriers of hydrides are reduced as the solid solution of hydrogen atom increases in nanoparticles, lowering the apparent activation energies of the hydriding/dehydriding reactions in Mg-based hydrogen storage materials [65,119–122].

Mg nanoparticles obtained by high-energy ball-milling process do not require the initial activation. Furthermore, it possesses fast hydrogenation and de-hydrogenation rate than bulk polycrystalline Mg, as reported by Schulz et al. [123]. Nanocrystalline Mg can be fully hydrogenated within 6.5 min and desorb within 1 h at 300 °C. These are in stark contrast to the bulk Mg, in which de-hydrogenation hardly occurs at the same temperature. Compared with polycrystalline Mg, the apparent activation energies of the hydriding/dehydriding reactions decrease to 40~60 kJ/mol [124]. It is unveiled that [16,125–128] ball-milling process enhances the surface area of fresh Mg, reducing the effect of surface impurity, such as MgO, etc. The defects on surface of Mg will promote H_2 dissociation. In addition, the kinetic properties are simply improved by enhancing surface area, i.e., the specific surface area is increased by 10 times after the ball-milling process. All of the aforementioned strategies promote the dissociation of hydrogen molecules and the diffusion of hydrogen atoms, improving overall kinetic properties.

However, the particle size of the nano-crystalline Mg after several hydrogenation/de-hydrogenation cycles increases from a few nanometers to a few hundred nanometers due to the aggregation effect [129]. Moreover, the surface defects disappear during the annealing process. However, from the view of kinetic behavior of hydrogen absorption and desorption processes, the decay of kinetic performance is not significant, implying that the improved kinetics are likely free from the influence of defects and stresses produced in the ball milling process [130]. The origin of the improved kinetics is considered as the decreased particle size results in shortened diffusion length. Besides, the active reaction interface is increased by suppressing the surface magnesium oxide layer.

Inspired by the improvement in kinetics of hydriding/dehydriding reactions in Mg/MgH₂ by reducing particle size, substantial investigations regarding nano-sized Mg (zero-dimensional (0D) nanodots, 1D nanowires, and 2D nanofilms) were conducted [132–134]. Qu et al. [135] investigated Mg nanowires with different thickness synthesized by vapor deposition. The results show that hydrogen can be absorbed on the nanowires at nearly room temperature, but the de-hydrogenation temperature is still high. The kinetic performance decays fast due to the change of film structure after several hydrogenation/de-hydrogenation processes. Li et al. [131] found that the activation energies of hydriding/dehydriding reactions in 30–50 nm Mg nanowire decrease to 33.5–38.8 kJ/mol. Moreover, the uptake/release activation energies were suppressed with decreasing nanowire diameter (Fig 9).

However, although most of the studies report a significant improvement on the hydrogen absorption performance of Mg-based materials based on nano-crystallization method, the de-hydrogenation temperature and dehydriding rate are still far behind our expectations. Furthermore, the high surface energy of nano-materials makes them easily to agglomerate, challenging to maintain good kinetic performance. Since the dissociation and recombination of hydrogen are the critical steps to improve the kinetic performance of Mg-based hydrogen storage materials, employing catalysts to decrease the energy barriers is becoming a more promising approach.

3.2.2. Catalysis

Hydrogen dissociation and recombination are the critical steps for H_2 storage materials. Vegge investigated the H_2 dissociation/desorption and diffusion processes of dissociated hydrogen atoms on Mg (0001) plane using density functional theory [136]. It was found that hydrogen dissociation shows the highest energy barrier for the activation of hydrogen molecules, which was estimated to be 1.15 eV. While other energy barrier can also be identified between the meta-stable state and the final state, which is less critical because of the much smaller activation energy. Therefore, using catalyst is an effective way to improve the kinetic performance of chemical reactions. Both of the hydrogenation/de-hydrogenation kinetics can be significantly improved by enhancing the dissociate and recombine rate of hydrogens with catalyst. In addition,

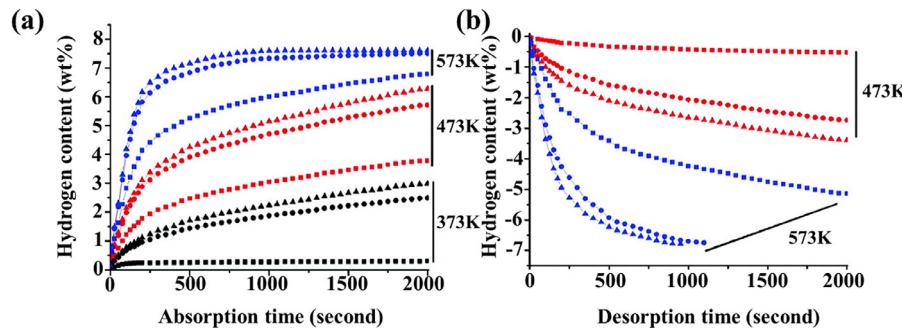


Fig. 9. The (a) hydrogenation and (b) de-hydrogenation rates as the function of time of Mg nano-wires with different diameters. The black, red and blue points are the data collected at 373 K, 473 K and 573 K, respectively. [131].

the catalyst can also help to improve H diffusion as a "hydrogen pump".

The effect of transition metals (*TM*) as catalysts on the hydriding and dehydriding reactions in MgH_2 was extensively investigated by researchers, because of their variable valence states and excellent catalytic effects [137,138]. Xia et al. [139] reported a bottom-up self-assembly MgH_2 nanoparticles anchored on graphene uniformly with a loading ratio high to 75 wt %. After modified with Ni catalyst, the graphene supported MgH_2 presented superior hydrogen absorption/desorption properties, hydrogenating/ dehydrogenating completely at 50 °C and 200 °C, respectively. The superior hydrogen storage properties of MgH_2 were further observed by porous Ni nanofibers catalyzed MgH_2 . The 4% Ni nanofibers catalyzed MgH_2 starts to release hydrogen at only 143 °C, with a peak temperature of 244 °C [140]. Liang et al. [141] systematically investigated the catalytic effect of early to late transition metals on Mg/ MgH_2 system. The authors prepared the MgH_2-TM ($TM = Ti, V, Mn, Fe$, and Ni) using the ball-milling method. The results show that Ti and V possess good catalytic effect among the above-studied transition metals. The activation energies of the hydrogen desorption process were estimated to be 71.1 kJ/mol for MgH_2-Ti , 62.3 kJ/mol for MgH_2-V , 104.6 kJ/mol for MgH_2-Mn , 67.6 kJ/mol for MgH_2-Fe , and 88.1 kJ/mol for MgH_2-Ni , respectively. The obtained activation energies are smaller than the ball-milled MgH_2 sample (120 kJ/mol). Cui et al. employed chemical reaction between Mg metal and $TMCl_x$ ($TiCl_3$, $NbCl_5$, VCl_3 , $CoCl_2$, $MoCl_3$, $NiCl_2$) to load nano-sized transition metals on Mg/ MgH_2 [142]. In this study, Mg-TM composites were synthesized using metal Mg and $TMCl_x$ as the precursors. It was reported that 10–20 nm-sized TMs are dispersed on Mg surface after the reaction in tetrahydrofuran, resulting in a core-shell-like structure. The activation energy of de-hydrogenation was reduced to be 30.9 kJ/mol for MgH_2-Ti system [142].

The catalytic activity can be scaled as a function of *Me-H* interaction, where *Me* indicates metal catalysts, known as a volcano plot (Fig. 10) [143]. The catalytic activity shows the highest value for the noble metals having moderate *Me-H* interaction while degrading with increasing or decreasing *Me-H* interaction. The tendency can be interpreted as follows: The stronger *Me-H* interaction represents a higher binding

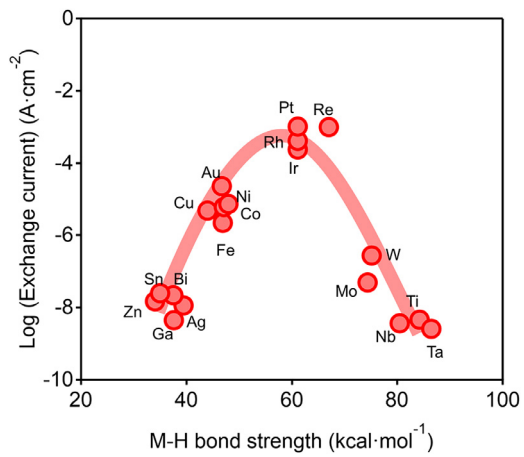


Fig 10. The volcano plot for hydrogen evolution reaction [143]. The x and y-axis represent M-H bond formation energy and catalytic activity, respectively.

energy between hydrogen and catalysts and thus more thermal energy is needed to break *Me-H* bonding to stimulate a further reaction. Meanwhile, the weak *Me-H* interaction is difficult to adsorb H on catalyst, therefore, the *Me* cannot serve as catalysts that promote hydrogen's activation, recombination and diffusion.

The results of the catalytic effects on Mg/ MgH_2 raise the following question: Why some reports show that the catalytic effect of Ni (a famous hydrogenation catalyst) is lower than Ti or other transition metals? To solve the problem, Han et al. systematically investigated the impact of Ni on the (0001) surface and bulk metal of Mg. [136], where 6 Ni positions were taken into account, i.e., three sites are on the surface (FCC site, HCP site, and Bridge site) and other three sites are located in the 1st, 2nd, and 3rd layers, respectively. The activation energies of hydrogen dissociation on Mg (0001) plane were estimated to be 1.4 eV, in consistent with the values reported by Vegge (1.2 eV) [144]. Interestingly, the activation energies were suppressed to 0.04–0.05 eV when Ni is located on the surface and the 1st layer of Mg [136]. The activation energies of surface diffusion increase when Ni is located on the surface, due to the relative strong Ni-H interaction. Thus, more thermal energy is required to break the chemical bond, and the activation energy changed from

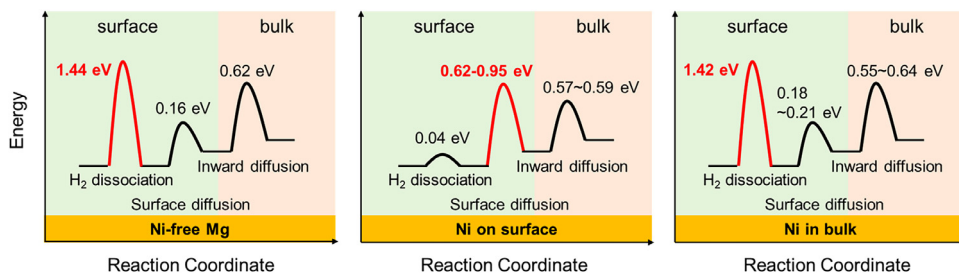


Fig 11. The energy modification and reaction coordinate of each model. Hydrogen dissociation and diffusion process of Ni-free Mg (0001) surface, Ni on Mg (0001) surface and Ni in Mg bulk were considered, respectively [136].

0.16 eV (Ni-free) to 0.62–0.95 eV (Ni on the surface). In these cases, the surface diffusion becomes the rate-determine step rather than hydrogen dissociation (Fig 11). The activation energies of inward diffusion almost remain unchanged after migrating Ni in the bulk structure of Mg.

These results indicate that the three essential steps are strongly correlated each other and all of the steps must be considered during the hydrogenation/de-hydrogenation processes. Namely, the real reaction is much more complicated than the well-studied hydrogenation models. Thus, it is required to establish new scaling relations for hydrogen storage materials in future. The above discussion is based on the simple combination of elemental Mg and Ni, and cannot be used to the Mg-Ni binary alloys and intermetallic systems. For example, Cho et al. [145] reported that both thermodynamic and kinetic properties could be significantly improved using Mg-Ni binary nanoalloys as additives to the Mg/MgH₂ system. It is not surprising, because Mg-Ni binary compounds exhibit different crystal and electronic structures, resulting in distinct M-H interactions.

3.2.3. The other sample preparation technology

Hydring combustion synthesis. Based on the hydring combustion synthesis (HCS) method, various Mg-based materials showing superb hydrogen storage performance have been prepared by Li and Zhu et al. [39,50,126,146,147]. Binary Mg-Al [148], Mg-Ni [149], ternary Mg-Ni-La [150], Mg-Ni-Fe [151], and other Mg-based composites were synthesized in the HCS process. For example, Mg@Ni/Gn (Gn: Graphene nanoplate) samples were successfully synthesized by this method using the mixture of Mg and Ni/Gn additives. The Mg@Ni₈Gn₂ absorbed 6.28 wt.% hydrogen within 100 s at 100 °C, which can be explained by the uniform dispersion of in situ formed Mg₂NiH₄ nanoparticles [152]. Without activation process, Mg-Ni composite synthesized by HCS (HCSed Mg₈₀Ni₂₀) can release hydrogen at ca. 210 °C, indicating that the HCS method can be applied to the metal-based hydrides with high activity [153]. In addition, abundant methods such as surface modifying [154], compositing [155], and catalyzing [156] were applied to enhance the hydrogen storage performance of HCSed Mg-based materials. For example, bulk Mg-Ni-based hydrides with rapid treatment by water exhibit peak dehydrogenation temperature at 108 °C. Simultaneously, the air stability is improved due to the in situ formed

Ni@Mg(OH)₂ nanosheets [154]. HCSed MgH₂+LiAlH₄ composite shows faster dehydrogenation kinetics and lower dehydrogenation barrier than commercial MgH₂+LiAlH₄ composite, indicating the pronounced synergistic effect brought by the unique structure of HCSed MgH₂ [157]. After introducing Ni₃₀/FL-Ti₃C₂T_x (FL: few layer) catalyst, HCSed MgH₂ desorbs 5.83 wt.% hydrogen within 1800s at 250 °C because of the rich electronic interaction brought by the sufficient contacts and interfaces between Ni nanoparticles and Ti₃C₂ matrix [158].

Amorphization. As structural materials, metallic glasses (MGs) or amorphous alloys have attracted great attention due to their high strength, high hardness, excellent corrosion resistance, etc. [159–162] which are rendered by their unique uniform disordered atomic structure compared to their crystal counterparts [161–164]. In addition, MG has also been widely used as functional materials, for example, in the hydrogen storage realm as hydrogen storage materials that directly possess higher capacity due to their large free volume [165].

Amorphous Mg-based alloys, particularly Mg-La-Ni amorphous alloys, were firstly prepared by Inoue group in the 1990s [166]. Afterward, tremendous efforts have been devoted to study the hydrogen storage properties of amorphous Mg-based alloys prepared by melt-spinning. Spassov et al. [167,168] reported that some nanocrystalline and/or amorphous Mg-rare earth (RE)-Ni alloys showed much superior hydrogen absorption/desorption properties than the corresponding conventional crystalline alloys. They found that the melt-spun Mg₇₅Ni₂₀RE₅ (RE = Ce or La-rich mischmetal) alloy possesses fast hydrogenation kinetics with a hydrogen capacity of ~4 wt.% by searching a series of Mg-RE-Ni alloys. Kalinichenko et al. [169] reported the hydrogen storage properties of melt-spun Mg-based alloys, including Mg₉₀Cu_{2.5}Ni_{2.5}Y₅, Mg₈₅Cu₅Ni₅Y₅, and Mg₈₀Cu₅Ni₅Y₁₀. The activation procedure and the hydrogen sorption kinetics of these alloys were studied by thermogravimetric analysis at different temperatures in the range from 100 °C to 380 °C, these alloys can reach up to reversible gravimetric H₂ storage of 4.8 wt.%.

The hydrogen storage capacity of Mg-based alloys depends on the content of Mg elements in the alloys. On one hand, RE or Ni elements benefit to enhance the glass-forming ability

(GFA) of Mg-based alloys and the hydrogen storage kinetics of MgH_2 . On the other hand, Ni and RE are much heavier than Mg, which reduces the hydrogen storage capacity of Mg-based alloys. Therefore, Ni and RE contents should be rationally controlled in a suitable window. Lin et al. [56] studied the effect of Ce and Ni contents on the GFA of Mg-Ce-Ni system on Mg-rich corner of phase diagram by X-ray diffraction (XRD) patterns and differential scanning calorimetry (DSC) curves of the melt-spun alloys. As a result, the melt-spun $\text{Mg}_{90}\text{Ce}_5\text{Ni}_5$ amorphous alloy with the highest Mg-content in this system shows rapid hydrogenation kinetics. At 300 °C, about 5.0 wt.% H can be absorbed within 5 min, reaching the reaction rate of 1 wt.%-H/min. The onset dehydrogenation temperature of the amorphous $\text{Mg}_{90}\text{Ce}_5\text{Ni}_5$ alloy is ~50 °C lower than that of the induction-melt crystalline alloy. Moreover, the activation energies of MgH_2 desorption for melt-spun and induction-melt $\text{Mg}_{90}\text{Ce}_5\text{Ni}_5$ alloys are 109.2 kJ/mol and 124.6 kJ/mol, respectively. Lin et al. [170] also found that increasing hydrogen gas pressure and reducing temperature are beneficial for obtaining fine hydrides with lowered hydrogen desorption temperature and activation energy. The activation energy of MgH_2 desorption for the cycled sample induced by the highest pressure and the lowest temperature is only 87 ± 7 kJ/mol, which is much smaller than that of the cycled sample induced by the lowest pressure and the highest temperature (98 ± 8 kJ/mol).

However, the amorphous Mg-based alloys usually encounter crystallization during the hydrogenation and dehydrogenation processes which requires high temperature and high hydrogen pressure. To avoid crystallization, Lin et al. [165,171–174] studied the hydrogen storage properties of Mg-Ce-Ni alloys at temperature as low as 25–120 °C. At room temperature, the hydrogenation kinetics curve of Mg-Ce-Ni alloys can be fitted by Avrami-Erofeev equation deduced from the nucleation and growth process.

$$\alpha = 1 - \exp(-Bt^m) \quad (22)$$

where α is the weight ratio of reacted material to total material, m and B are constants relating with temperature and nucleation rate, respectively. The rate-determining step of hydrogenation kinetics of the $\text{Mg}_{90}\text{Ce}_5\text{Ni}_5$ amorphous alloy at 25 °C is likely to be a diffusion process, indicating that hydrogen penetrates directly into the amorphous alloy under high pressure. Hydrogenation kinetics of the amorphous $\text{Mg}_{80}\text{Ce}_{10}\text{Ni}_{10}$ powders under an initial pressure of 4.5 MPa at 120 °C are shown in Fig. 12. The amorphous $\text{Mg}_{80}\text{Ce}_{10}\text{Ni}_{10}$ alloy absorbs hydrogen with sluggish kinetics in the initial 15 h and then, the absorption rate further slows down, resulting in over 80 h to reach full hydrogenation (~5.0 wt.%-H). Fig. 12b shows the evolution of XRD patterns as increasing hydrogen concentration. The $\text{Mg}_{80}\text{Ce}_{10}\text{Ni}_{10}$ amorphous alloy displays a broad amorphous peak at 2θ of 35°. With the increase in hydrogen concentration, the diffraction peak at 35° decreases in intensity. Meanwhile, a new diffraction peak at 29° appears after charging of 5 wt.%-H (i.e. H/M = 2.07). The reduced diffraction peak angle suggests that the space between atoms in the amorphous matrix considerably expands

upon hydrogenation. High-angle annular dark-field scanning transmission electron microscopy (HAADF-STEM) measurements were performed to directly observe the atom-scale structure of the $\text{Mg}_{80}\text{Ce}_{10}\text{Ni}_{10}$ amorphous alloy and hydride, as shown in Fig. 12c-d. The acquired HAADF-STEM images give very clear information that the image contrast is approximately proportional to the square of the atomic number. The disordered atoms in amorphous alloy and hydride are distinguishable in the STEM images. The size of the disordered Ce/Ni clusters in the amorphous alloy is a few nanometres; however, these clusters remarkably grow upon hydrogenation.

3.2.4. External field

The magnetic field is an external factor that can affect the free energy of materials through the interaction with electron-spin, which is known as the Zeeman effect. Strong magnetic field (e.g., 10 T) is possibly to change the microscopic structure of materials, including atomic order, coordination, and migration without mechanical contact. Therefore, their physical properties can be significantly optimized [175–177]. The Gibbs free energy change associated with the applied magnetic field can be expressed as follows;

$$\Delta G_{M \rightarrow MH_2}^{mag} = (G_{MH_2}^{mag} - G_M^{mag}) - (E_{MH_2}^{mag} - E_M^{mag}) \quad (23)$$

where G_ϕ^{mag} is the contribution of free energy derived from the magnetic field to the phase. According to the Hillert-Jah and Inden model, G_ϕ^{mag} is considered as the function of magnetic moment m , which is proportional to the applied external field. The G_ϕ^{mag} can be expressed as,

$$E_\phi^{mag} = \int_0^B m(T, B) dB, \quad (24)$$

where B is the magnitude of the external magnetic field. To investigate the effect of the magnetic field in hydrogen storage materials, an experimental device combined with magnets was developed by Li et al. [178,179]. A static magnetic field, varying from 0 to 14 T, can be generated in this device. Nanostructured Mg_2FeH_6 was successfully prepared by this method. Here we name the technique as controlled hydrogenation combustion synthesis under the high magnetic field (CHCS) [180]. Compared to the sample synthesized by the conventional HCS method, the CHCS technique affects the structure and morphological characteristics, phase composition, crystal size, as well as elemental distribution of the Mg-Fe and Mg-LaNi_x composites, successfully decreasing the hydrogenation/de-hydrogenation temperature. Electrochemical functionalities of $\text{La}_{0.67}\text{Mg}_{0.33}\text{Ni}_{2.5}\text{Co}_{0.5}$ alloy, synthesized by CHCS technique, were investigated [48,181]. The results show that the (La, Mg)Ni₃ transforms to the (La, Mg)₂Ni₇ structure alongside the unit cell expansion. Similar synthesis method was also applied to $\text{Mg}_2\text{Ni}_{0.8}\text{Mn}_{0.2}$. [182]

Besides, the microwave is also applicable to assist the phase formation. Liu et al. [183] applied magnetic field and microwave during the sample preparation and investigated their effects on material thermodynamics and kinetics. Li et al. [184] investigated the microwave-assisted synthesis of Mg-La-Ni alloy and investigated its crystallography and hydro-

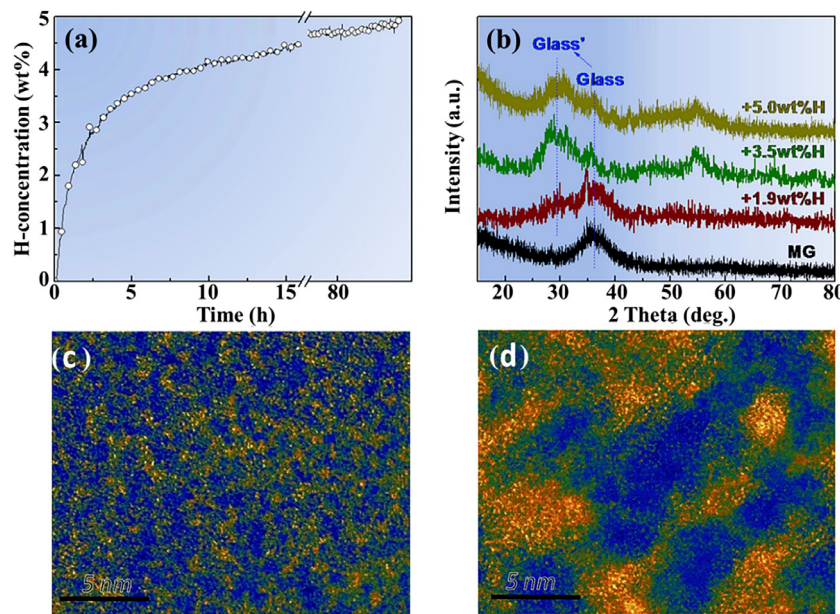


Fig. 12. (a) Hydrogenation kinetic curve of $\text{Mg}_{80}\text{Ce}_{10}\text{Ni}_{10}$ amorphous alloy, (b) XRD patterns of $\text{Mg}_{80}\text{Ce}_{10}\text{Ni}_{10}$ amorphous alloy with the increase of hydrogen concentration. HAADF STEM images of $\text{Mg}_{80}\text{Ce}_{10}\text{Ni}_{10}$ amorphous alloy (c) before and (d) after full hydrogenation. The figures are reproduced from Ref. [171].

gen storage properties. The P-C-T results show that the reaction enthalpy of synthesized composite (Mg 60.00 wt.%; La 12.96 wt.%; Ni 27.04 wt.%) is comparable to Mg-Ni-RE alloys, indicating that microwave-assisted synthesis can improve the thermodynamic properties of hydrogen storage materials. Meng et al. [52,185] comparatively studied the effect of microwave-assisted and conventional solid-state reactions on the properties of Nd-Mg-Ni- Fe_3O_4 alloy. The hydrogen storage capacity of the samples prepared by conventional methods was less than 5.0 wt.% at 280–350 °C, while the one made by microwave-assisted synthesis exhibits a higher hydrogen storage capacity (over 5.5 wt.%) and wider plateau region of hydrogenation/de-hydrogenation processes. In addition, the hydrogenation enthalpy and entropy are slightly lowered by this technique. Luo et al. compared the effects of magnetic and microwave fields on the kinetic characteristics of self-made Mg_2Ni hydrogen storage alloys [92]. The external fields have a positive influence on both thermodynamic and kinetic properties of Mg_2Ni . Especially, the kinetic properties of the sample prepared by microwave-assisted activation-synthesis are significantly improved. The enhanced hydriding/dehydriding kinetic properties can be ascribed to the formation of the new structure and the incident energy into materials from the physical field, leading to a decrease of reaction activation energy.

Overall, both the magnetic field- and microwave-assisted preparation can optimize the microstructure and particle size of the alloy. Namely, the above technique contributes to optimizing the macroscopic morphology of the structure, while the phase itself remained unchanged. However, few attempts have been carried out to couple the electric, magnetic, microwave, ultrasonic, and even mechanical fields to obtain better kinetics properties.

4. Summary and outlook

4.1. Summary

As a solution for the inescapable problem of H_2 storage, Mg-based materials hold outstanding merits of good capacity, meeting the DOE ultimate target, etc., but limited by slow thermodynamics and kinetics (High dehydrogenation temperature and low H_2 release rate). The temperature, enthalpy, and entropy, etc. play significant roles in determining the reaction thermodynamics. The P-C-T curve can be obtained by calculating the Gibbs free energies.

The recent progress of kinetic behaviors of Mg-based H_2 storage materials are also reviewed. Particularly, four kinetic steps (physisorption, chemisorption, penetration and diffusion, nuclear and growth) as well as their rate-determining factors are detailed summarized. Various geometrical contraction models, e.g., Jander model, G-B model, V-C model, etc., were discussed based on the hypothesis that hydrogen diffusion is the rate-determining step. In addition, a classical JMAK model was discussed to analyses the nucleation and growth of β phase. On the basis of these models, the activation energy, release rate, penetration process of H_2 , nucleation and growth of β phase as well as the phase interface migration, etc. could be accurately predicted. To improve the kinetics of Mg-based H_2 storage materials, various strategies were adopted to lowering the energy barrier or create new diffusion path, including ball milling, catalyst addition, core-shell structure, using external field, etc. These approaches improve the hydrogen absorption/desorption behavior and are helpful for further development of Mg-based hydrogen storage materials.

In summary, great efforts have been devoted to study the thermodynamics and kinetics of H_2 storage materials so far.

Despite the numerous achievements, some challenges remain unsolved. When the H₂ storage materials can be commercialized is still an open question.

4.2. Outlook and challenge

A variety of studies revealed the effectiveness of nanocrystallization and catalytic effects to improve the thermodynamic and kinetic properties of Mg-based H₂ storage materials. However, prior to the commercialization, several inescapable barriers need to be overcome:

- (1) The mechanism of enhanced thermodynamics and kinetics of doping TMs into Mg/MgH₂ remains unclear. Moreover, few studies are reported on the multiple elements doping/alloying (e.g., B, C, ect.). As the energy-electron contribution is insufficient to describe the full enthalpy at finite temperature, the synergistic effect from electronic, magnetic, and vibrational excitations should be properly described.
- (2) Hydrogen dissociation, surface diffusion and surface penetration are three critical steps in H₂ storage process in terms of large activation energy barrier. An “overall consideration” on the three steps in material design needs special attention in future. For example, Ni-based catalysts can enable hydrogen dissociation by lowering the reaction barrier, but limited hydrogen diffusion on catalyst surface due to the solid Ni-H bonding.
- (3) Downsizing particle size is effective way to improve both thermodynamics and kinetics by increasing surface area and energies. However, most of the Mg-based materials are sensitive to air and moisture, which will deteriorate their performance. Furthermore, the relatively short cycle-life induced by aggregation and particle growth during the hydrogenation/dehydrogenation should be addressed. Combining Mg-based nanoparticles on large specific area materials could to be a promising research direction to solve the problem.
- (4) The mechanisms for the influence of elemental substitution/doping, and catalyst on enthalpy, P-C-T curve and hysteresis coefficient of hydrogen absorption and desorption remain unclear. While DFT calculations can provide the deep insight into the mechanism of the hydrogenation and dehydrogenation process of simple systems (e.g., pure Mg and MgH₂), the models and strategies adopting to complex systems need to be amended, such as multiple elements alloying, multiple external fields, and nano-sized structures. For more troublesome and complicated systems (e.g., elemental substitution/doping, alloying, nano-crystallinity, catalyst addition, and chemical modification), additional theoretical and experimental efforts are required to provide comprehensive understandings.

Acknowledgements

This work was supported by the Chongqing Special Key Project of Technology Innovation and Application Development, China ([cstc2019jscx-dxwtB0029](#)), the National Natural Science Foundation of China (51871143), the Science and Technology Committee of Shanghai (19010500400), the Shanghai Rising-Star Program (21QA1403200), Chongqing Research Program of Basic Research and Frontier Technology (No. [cstc2019jcyj-msxmX0306](#)), the Start-up Funds of Chongqing University (02110011044171), the Senior Talent Start-up Funds of Jiangsu University (4111310024) and the Independent Research Project of State Key Laboratory of Mechanical Transmissions ([SKLMT-ZZKT-2021M11](#)). Qian Li acknowledges Dr. Chao Yang for discussion on the kinetics of hydriding and dehydriding reactions.

References

- [1] J. Yang, Y. Zhao, J. Cao, C.P. Nielsen, Environ. Int. 152 (2021) 106482.
- [2] J. Liu, M. Murshed, F. Chen, M. Shahbaz, D. Kirikkaleli, Z. Khan, Sustain. Prod. Consum. 26 (2021) 943–957.
- [3] J.P. Lopes, P.M.R. Almeida, F.J. Soares, Using vehicle-to-grid to maximize the integration of intermittent renewable energy resources in islanded electric grids, proceedings of the 2009 International Conference on Clean Electrical Power, F 9-11 June 2009, 2009 [C].
- [4] D. Huston, Safety and operations of hydrogen fuel infrastructure in northern climates: a collaborative complex systems approach (2010)
- [5] A. Züttel, Naturwissen 91 (2004) 157–172.
- [6] T. Graham, Proc. R. Soc. London 17 (1869) 212–220.
- [7] A. Züttel, Mater. Today 6 (2003) 24–33.
- [8] T.K. Nielsen, F. Besenbacher, T.R. Jensen, Nanoscale 3 (2011) 2086–2098.
- [9] L. Wang, R.T. Yang, Energy Environ. Sci. 1 (2008) 268–279.
- [10] X. Yu, Z. Tang, D. Sun, L. Ouyang, M. Zhu, Prog. Mater. Sci. 88 (2017) 1–48.
- [11] J. Song, J. She, D. Chen, F. Pan, J. Magnes. Alloy. 8 (2020) 1–41.
- [12] Y. Yang, X. Xiong, J. Chen, X. Peng, D. Chen, F. Pan, J. Magnes. Alloy. 9 (2021) 705–747.
- [13] D.A. Sheppard, C.E. Buckley, Int. J. Hydrogen Energy 44 (2019) 9143–9163.
- [14] Y. Tang, Y. Li, W. Zhao, I. Roslyakova, L. Zhang, J. Magnes. Alloy. 8 (2020) 1238–1252.
- [15] V. Bérubé, G. Radtke, M. Dresselhaus, G. Chen, Int. J. Energy Res. 31 (2007) 637–663.
- [16] X. Hou, H. Shi, L. Yang, K. Hou, Y. Wang, L. Feng, G. Suo, X. Ye, L. Zhang, Y. Yang, J. Magnes. Alloy. 9 (2021) 1068–1083.
- [17] J. Zhang, S. Yan, G. Xia, X. Zhou, X. Lu, L. Yu, X. Yu, P. Peng, J. Magnes. Alloy. 9 (2021) 647–657.
- [18] J. Bai, H. Xie, X. Pang, G. Yuan, L. Wang, Y. Ren, G. Qin, J. Mater. Sci. Technol. 79 (2021) 133–140.
- [19] Y. Guo, Y. Li, B. Liu, W. Liu, X. Liang, Q. Gu, Q. Li, J. Alloys Compd. 750 (2018) 117–123.
- [20] Y. Guo, Q. Luo, B. Liu, Q. Li, Scripta Mater. 178 (2020) 422–427.
- [21] S.A. Shevlin, Z.X. Guo, Chem. Soc. Rev. 38 (2009) 211–225.
- [22] P. Hohenberg, W.J.P.R. Kohn 136 (1964) B864.
- [23] W. Kohn, L.J. Sham, Phys. Rev. 140 (1965) A1133–A1138.
- [24] Q. Luo, J. Li, B. Li, B. Liu, H. Shao, Q. Li, J. Magnes. Alloy. 7 (2019) 58–71.
- [25] R.W.P. Wagelmans, J.H. Van Lenthe, P.E. De Jongh, A.J. Van Dillen, K.P. De Jong, J. Am. Chem. Soc. 127 (2005) 16675–16680.
- [26] S. Cheung, W.-Q. Deng, A.C.T. Van Duin, W.A. Goddard, J. Phys. Chem. A. 109 (2005) 851–859.

- [27] K.C. Kim, B. Dai, J. Karl Johnson, D.S. Sholl, *Nanotechnology* 20 (2009) 204001.
- [28] S. Rameshkumar, G. Jaiganesh, V. Jayalakshmi, *J. Magnes. Alloy.* 7 (2019) 166–185.
- [29] Z. Wu, L. Zhu, F. Yang, Z. Jiang, Z. Zhang, *J. Alloys Compd.* 693 (2017) 979–988.
- [30] Z. Wu, L. Zhu, F. Yang, Z. Zhang, S.N. Nyamsi, *Eur. Phys. J. B* 91 (2018) 73.
- [31] S. Kumar, A. Jain, H. Miyaoka, T. Ichikawa, Y. Kojima, *Int. J. Hydrogen Energy* 42 (2017) 17178–17183.
- [32] S. Kumar, A. Singh, G.P. Tiwari, Y. Kojima, V. Kain, *Thermochim. Acta* 652 (2017) 103–108.
- [33] Z. Wu, L. Zhu, F. Yang, Z. Jiang, Z. Zhang, *Int. J. Hydrogen Energy* 41 (2016) 18550–18561.
- [34] L. Ouyang, F. Liu, H. Wang, J. Liu, X.-S. Yang, L. Sun, M. Zhu, *J. Alloys Compd.* 832 (2020) 154865.
- [35] H.C. Zhong, H. Wang, J.W. Liu, D.L. Sun, M. Zhu, *Scripta Mater.* 65 (2011) 285–287.
- [36] H. Wang, Z. Haichang, L. Ouyang, J. Liu, D. Sun, Q. Zhang, M. Zhu, *J. Phys. Chem. C* 118 (2014) 12087–12096.
- [37] J. Mao, T. Huang, S. Panda, J. Zou, W. Ding, *Chem. Eng. J.* 418 (2021) 129301.
- [38] R.H. Reilly Jr, *Inorg. Chem.* 7 (1968) 2254–2256.
- [39] M. Zhu, Y. Lu, L. Ouyang, H. Wang, *Materials* (Basel, Switzerland) 6 (2013) 4654–4674.
- [40] Q. Li, Q. Lin, L.J. Jiang, K.C. Chou, F. Zhan, Q. Zheng, X.Y. Wei, *J. Alloys Compd.* 359 (2003) 128–132.
- [41] Q. Li, Q. Lin, K.C. Chou, L.J. Jiang, K.D. Xu, *J. Alloys Compd.* 397 (2005) 68–73.
- [42] Q. Li, L.J. Jiang, K.C. Chou, Q. Lin, F. Zhan, K.D. Xu, X.G. Lu, J.Y. Zhang, *J. Alloys Compd.* 399 (2005) 101–105.
- [43] Y. Takahashi, H. Yukawa, M. Morinaga, *J. Alloys Compd.* 242 (1996) 98–107.
- [44] H. Yang, H. Yuan, J. Ji, H. Sun, Z. Zhou, Y. Zhang, *J. Alloys Compd.* 330–332 (2002) 640–644.
- [45] M. Ismail, M.S. Yahya, N.A. Sazelee, N.A. Ali, F.H. Yap, N.S. Mustafa, *J. Magnes. Alloy.* 8 (2020) 832–840.
- [46] P. Yao, Y. Jiang, Y. Liu, C. Wu, K.C. Chou, T. Lyu, Q. Li, *J. Magnes. Alloy.* 8 (2020) 461–471.
- [47] L.Z. Ouyang, F.X. Qin, M. Zhu, *Scripta Mater.* 55 (2006) 1075–1078.
- [48] X. Zhao, Q. Li, K. Chou, H. Liu, G. Lin, *J. Alloys Compd.* 473 (2009) 428–432.
- [49] K.-B. Wu, Q. Luo, S.L. Chen, Q.F. Gu, K.C. Chou, X.L. Wang, Q. Li, *Int. J. Hydrogen Energy* 41 (2016) 1725–1735.
- [50] Q. Li, Q. Lin, L. Jiang, K.-C. Chou, *J. Alloys Compd.* 368 (2004) 101–105.
- [51] Q. Li, L.W. Ye, J. Meng, Y. Liu, K.C. Chou, *J. Alloys Compd.* 509 (2011) 99–104.
- [52] J. Meng, X.L. Wang, K.C. Chou, Q. Li, *Metall. Trans. A* 44 (2013) 58–67.
- [53] K. Xu, S. Liu, K. Chang, Y. Liang, Y. Du, Z. Jin, *J. Magnes. Alloy.* 9 (2021) 144–155.
- [54] Y. Zhou, P. Mao, L. Zhou, Z. Wang, F. Wang, Z. Liu, *J. Magnes. Alloy.* 8 (2020) 1176–1185.
- [55] J.W. Liu, C.C. Zou, H. Wang, L.Z. Ouyang, M. Zhu, *Int. J. Hydrogen Energy* 38 (2013) 10438–10445.
- [56] H.J. Lin, L.Z. Ouyang, H. Wang, D.Q. Zhao, W.H. Wang, D.L. Sun, M. Zhu, *Int. J. Hydrogen Energy* 37 (2012) 14329–14335.
- [57] Q. Luo, Q.F. Gu, J.Y. Zhang, S.L. Chen, K.C. Chou, Q. Li, *Sci Rep* 5 (2015) 15385–15385.
- [58] L. Ouyang, X. Yang, M. Zhu, J. Liu, H. Dong, D. Sun, J. Zou, X. Yao, *J. Phys. Chem. C* 118 (2014) 7808–7820.
- [59] Q. Luo, Q. Gu, B. Liu, T.-F. Zhang, W. Liu, Q. Li, *J. Mater. Chem. A* 6 (2018) 23308–23317.
- [60] Q. Li, Y. Li, B. Liu, X. Lu, T. Zhang, Q. Gu, *J. Mater. Chem. A* 5 (2017) 17532–17543.
- [61] Y. Li, Q. Gu, Q. Li, T. Zhang, *Scripta Mater.* 127 (2017) 102–107.
- [62] Y.B. Pan, Y.-F. Wu, Q. Li, *Int. J. Hydrogen Energy* 36 (2011) 12892–12901.
- [63] H. Gu, Y. Zhu, L. Li, *Int. J. Hydrogen Energy* 34 (2009) 1405–1410.
- [64] T. Liu, C. Chen, C. Qin, X. Li, *Int. J. Hydrogen Energy* 39 (2014) 18273–18279.
- [65] Y. Pang, Q. Li, *Scripta Mater.* 130 (2017) 223–228.
- [66] E. Ianni, M.V. Sofianos, M.R. Rowles, D.A. Sheppard, T.D. Humphries, C.E. Buckley, *Int. J. Hydrogen Energy* 43 (2018) 17309–17317.
- [67] Y. Pang, Y. Liu, X. Zhang, M. Gao, H. Pan, *Int. J. Hydrogen Energy* 38 (2013) 1460–1468.
- [68] Y. Liu, Y. Pang, X. Zhang, Y. Zhou, M. Gao, H. Pan, *Int. J. Hydrogen Energy* 37 (2012) 18148–18154.
- [69] M.Y. Song, S.N. Kwon, Y. Kwak, H. Park, *Mater. Res. Bull.* 48 (2013) 74–78.
- [70] J. Jiang, J. Wei, H. Leng, Q. Li, K.-C. Chou, *Int. J. Hydrogen Energy* 38 (2013) 10919–10925.
- [71] L.P. Ma, Z.Z. Fang, H.B. Dai, X.D. Kang, Y. Liang, P.J. Wang, P. Wang, H.M. Cheng, *J. Mater. Res.* 24 (2009) 1936–1942.
- [72] B. Zhang, Y. Wu, *J. Alloys Compd.* 613 (2014) 199–203.
- [73] J.J. Vajo, S.L. Skeith, F. Mertens, *J. Phys. Chem. B* 109 (2005) 3719–3722.
- [74] R.A. Varin, T. Czujko, Z. Wronski, *Nanotechnology* 17 (2006) 3856–3865.
- [75] H. Shao, Y. Wang, H. Xu, X. Li, *Mater. Sci. Eng., B* 110 (2004) 221–226.
- [76] S. Ohno, M. Uda, *J. Japan Inst. Met. Mater.* 48 (1984) 640–646.
- [77] X. Zhang, R. Yang, J. Yang, W. Zhao, J. Zheng, W. Tian, X. Li, *Int. J. Hydrogen Energy* 36 (2011) 4967–4975.
- [78] Y. Lu, J. Li, T.N. Ye, Y. Kobayashi, M. Sasase, M. Kitano, H. Hosono, *ACS Catal.* 8 (2018) 11054–11058.
- [79] N. Norberg, T. Arthur, S. Fredrick, A. Prieto, *J. Am. Chem. Soc.* 133 (2011) 10679–10681.
- [80] W. Liu, K.F. Aguey-Zinsou, *J. Mater. Chem. A* 2 (2014) 9718–9726.
- [81] E.J. Setijadi, C. Boyer, K.F. Aguey-Zinsou, *Int. J. Hydrogen Energy* 38 (2013) 5746–5757.
- [82] V.Y. Gertsman, R. Birringer, *Scr. Metall. Mater.* 30 (1994) 577–581.
- [83] Y. Ben-Eliyahu, M. Brill, M.H. Mintz, *J. Chem. Phys.* 111 (1999) 6053–6060.
- [84] H. Wipf, *Phys. Scr.* T94 (2001) 43.
- [85] N. Gerard, *J. Less Common Met.* 131 (1987) 13–23.
- [86] M. Brill, J. Bloch, D. Shmariahu, M.H. Mintz, *J. Alloys Compd.* 231 (1995) 368–375.
- [87] Y. Ma, Y. Zhang, F. Liu, 14 (2021) 292.
- [88] K.F. Aguey-Zinsou, J.-R. Ares-Fernández, *Energy Environ. Sci.* 3 (2010) 526–543.
- [89] S. Ma, F. Xing, N. Ta, L. Zhang, *J. Magnes. Alloy.* 8 (2020) 819–831.
- [90] C. Cheng, X. Li, Q. Le, R. Guo, Q. Lan, J. Cui, *J. Magnes. Alloy.* 8 (2020) 1281–1295.
- [91] W. Jander, *Z. Anorg. Allg. Chem.* 163 (1927) 1–30.
- [92] Q. Luo, X.H. An, Y.B. Pan, X. Zhang, J.Y. Zhang, Q. Li, *Int. J. Hydrogen Energy* 35 (2010) 7842–7849.
- [93] A. Ginstling, B.J. Brounshtein, *Appl. Chem. USSR.* 23 (1950) 1327–1338.
- [94] R.E. Carter, *J. Chem. Phys.* 34 (1961) 2010–2015.
- [95] K.C. Chou, K. Xu, *Intermetallics* 15 (2007) 767–777.
- [96] K.C. Chou, Q. Li, Q. Lin, L.J. Jiang, K.D. Xu, *Int. J. Hydrogen Energy* 30 (2005) 301–309.
- [97] Y. Pang, Q. Li, Q. Li, Q. Luo, K.C. Chou, *Int. J. Hydrogen Energy* 41 (2016) 9183–9190.
- [98] Y. Pang, Q. Li, *Int. J. Hydrogen Energy* 41 (2016) 18072–18087.
- [99] K.C. Chou, Q. Luo, Q. Li, J.Y. Zhang, *Intermetallics* 47 (2014) 17–22.
- [100] Q. Li, X. Lin, ..Q. Luo, Y. Chen, J. Wang, B. Jiang, F. Pan, *Int. J. Miner. Metall. Mater.* (2021).
- [101] F. Liu, F. Sommer, C. Bos, E.J. Mittemeijer, *Int. Mater. Rev.* 52 (2007) 193–212.

- [102] F. Liu, F. Sommer, E.J. Mittemeijer, *Acta Mater.* 52 (2004) 3207–3216.
- [103] F. Liu, H. Nitsche, F. Sommer, E.J. Mittemeijer, *Acta Mater.* 58 (2010) 6542–6553.
- [104] F. Liu, C. Yang, G. Yang, Y. Zhou, *Acta Mater.* 55 (2007) 5255–5267.
- [105] F. Liu, F. Sommer, E.J. Mittemeijer, *J. Mater. Sci.* 39 (2004) 1621–1634.
- [106] Y. Che, C. Zhang, J. Song, X. Shang, X. Chen, J. He, *J. Magnes. Alloy.* 8 (2020) 752–760.
- [107] B. Hu, H.Q. Zhang, J. Zhang, Y.L. Liu, M.J. Yang, D. Zhao, *Acta Metall. Sin.* 57 (9) (2021) 1199–1214.
- [108] J. Escher, J. Pruess, G. Simonett, *J. Reine Angew. Math.* 2003 (2003) 1–52.
- [109] J.W. Morris, *Philos. Mag.* 90 (2010) 3–35.
- [110] Z. Pan, A. Lockley, *Microsc. Microanal.* 8 (2002) 1288–1289.
- [111] F. Liu, G. Yang, *Acta Mater.* 55 (2007) 1629–1639.
- [112] Y. Pang, D. Sun, Q. Gu, K.C. Chou, X.L. Wang, *Cryst. Growth Des.* 16 (2016).
- [113] L.J. Duan, Y.C. Liu, *Acta Metall Sin-Engl* 56 (2020) 112–118.
- [114] Y. Wu, C. Li, X. Xia, H. Liang, Q. Qi, Y. Liu, *J. Mater. Sci. Technol.* 67 (2021) 95–104.
- [115] P. Yang, C. Liu, Q. Guo, Y. Liu, *J. Mater. Sci. Technol.* 72 (2021) 162–171.
- [116] Y.C. Liu, F. Sommer, E.J. Mittemeijer, *Acta Mater.* 57 (2009) 2858–2868.
- [117] Y.C. Liu, F. Sommer, E.J. Mittemeijer, *Philos. Mag.* 84 (2004) 1853–1876.
- [118] X. Lin, H. Yang, Q. Zhu, Q. Li, *Chem. Eng. J.* 401 (2020) 126115.
- [119] G. Wu, J. Zhang, Q. Li, K. Chou, *Int. J. Hydrogen Energy* 36 (2011) 12923–12931.
- [120] J. Zhang, Y. Jian, X. Zhao, D. Meng, F. Pan, Q. Han, *J. Magnes. Alloy.* 9 (2021) 1187–1200.
- [121] M.S. Hasan, R. Lee, W. Xu, *J. Magnes. Alloy.* 8 (2020) 1296–1303.
- [122] M.U.F. Khan, A. Patil, J. Christudasjustus, T. Borkar, R.K. Gupta, *J. Magnes. Alloy.* 8 (2020) 319–328.
- [123] R. Schulz, J. Huot, G. Liang, S. Boily, G. Lalande, M.C. Denis, J.P. Dodelet, *Mater. Sci. Eng. A* 267 (1999) 240–245.
- [124] A. Zaluska, L. Zaluski, J.O. Ström-Olsen, *J. Alloys Compd.* 288 (1999) 217–225.
- [125] G.X. Wu, S.X. Liu, J.Y. Zhang, Y.Q. Wu, Q. Li, K.C. Chou, X.H. Bao, *Trans. Nonferrous Met. Soc. China* 19 (2009) 383–388.
- [126] Q. Li, Q. Lin, K.C. Chou, L.J. Jiang, F. Zhan, *Intermetallics* 12 (2004) 1293–1298.
- [127] P. Meena, R. Singh, V.K. Sharma, I.P. Jain, *J. Magnes. Alloy.* 6 (2018) 318–325.
- [128] N.A. Ali, M. Ismail, *J. Magnes. Alloy.* 9 (2021) 1111–1122.
- [129] O. Friedrichs, F. Aguey-Zinsou, J.R.A. Fernández, J.C. Sánchez-López, A. Justo, T. Klassen, R. Bormann, A. Fernández, *Acta Mater.* 54 (2006) 105–110.
- [130] H.G. Schimmel, M.R. Johnson, G.J. Kearley, A.J. Ramirez-Cuesta, J. Huot, F.M. Mulder, *J. Alloys Compd.* 393 (2005) 1–4.
- [131] W. Li, C. Li, H. Ma, J. Chen, *J. Am. Chem. Soc.* 129 (2007) 6710–6711.
- [132] M. Molaei, K. Babaei, A. Fattah-Alhosseini, *J. Magnes. Alloy.* 9 (2021) 1164–1186.
- [133] M. Shahin, K. Munir, C. Wen, Y. Li, *J. Magnes. Alloy.* 9 (2021) 895–909.
- [134] Y. Huang, G. Xia, J. Chen, B. Zhang, Q. Li, X. Yu, *Prog. Nat. Sci.* 27 (2017) 81–87.
- [135] J. Qu, Y. Wang, L. Xie, J. Zheng, Y. Liu, X. Li, *J. Power Sources* 186 (2009) 515–520.
- [136] Z. Han, Y. Wu, H. Yu, S. Zhou, *J. Magnes. Alloy.* (2021).
- [137] J. Cui, H. Wang, J. Liu, L. Ouyang, Q. Zhang, D. Sun, X. Yao, M. Zhu, *J. Mater. Chem. A* 1 (2013) 5603–5611.
- [138] L.Z. Ouyang, X.S. Yang, M. Zhu, J.W. Liu, H.W. Dong, D.L. Sun, J. Zou, X.D. Yao, *J. Phys. Chem. C* 118 (2014) 7808–7820.
- [139] G. Xia, Y. Tan, X. Chen, D. Sun, Z. Guo, H. Liu, L. Ouyang, M. Zhu, X. Yu, *Adv. Mater.* 27 (2015) 5981–5988.
- [140] J. Chen, G. Xia, Z. Guo, Z. Huang, H. Liu, X. Yu, *J. Mater. Chem. A* 3 (2015) 15843–15848.
- [141] G. Liang, J. Huot, S. Boily, A. Van Neste, R. Schulz, *J. Alloys Compd.* 292 (1999) 247–252.
- [142] J. Cui, J. Liu, H. Wang, L. Ouyang, D. Sun, M. Zhu, X. Yao, *J. Mater. Chem. A* 2 (2014) 9645–9655.
- [143] S. Trasatti, *J. Electroanal. Chem.* 39 (1972) 163–184.
- [144] T. Vegge, *Phys. Rev. B* 70 (2004) 035412.
- [145] E.S. Cho, A.M. Ruminski, Y.-S. Liu, P.T. Shea, S. Kang, E.W. Zaia, J.Y. Park, Y.-D. Chuang, J.M. Yuk, X. Zhou, T.W. Heo, J. Guo, B.C. Wood, J.J. Urban, *Adv. Funct. Mater.* 27 (2017) 1704316.
- [146] Q. Lin, L. Jiang, K.C. Chou, F. Zhan, Q. Zheng, *J. Mater. Sci. Technol.* (2004) 20.
- [147] Q. Li, K.-C. Chou, K.D. Xu, L.J. Jiang, Q. Lin, G.W. Lin, X.G. Lu, J.Y. Zhang, *Int. J. Hydrogen Energy* 31 (2006) 497–503.
- [148] S. Li, Y. Zhu, Y. Liu, Y. Zhang, H. Lin, J. Zhang, W. Qiu, L. Li, *J. Alloys Compd.* 819 (2020) 153020.
- [149] Y. Tan, Q. Mao, W. Su, Y. Zhu, L. Li, *RSC Adv.* 5 (2015) 63202–63208.
- [150] H. Gu, Y. Zhu, L. Li, *Int. J. Hydrogen Energy* 33 (2008) 2970–2974.
- [151] Y. Zhu, Y. Yang, L. Wei, Z. Zhao, L. Li, *J. Alloys Compd.* 520 (2012) 207–212.
- [152] J. Zhang, Y. Zhu, X. Zang, Q. Huan, W. Su, D. Zhu, L. Li, *J. Mater. Chem. A* 4 (2016) 2560–2570.
- [153] J. Zhang, L. Yao, W. Liu, Y. Zhu, R. Shi, Y. Zhang, Z. Ma, Y. Liu, H. Lin, L. Li, *Mater. Today Energy* 14 (2019) 100345.
- [154] R. Shi, H. Yan, J. Zhang, H. Gao, Y. Zhu, Y. Liu, X. Hu, Y. Zhang, L. Li, *Small* 17 (2021) 2100852.
- [155] Z. Ma, J. Liu, Y. Zhao, J. Zhang, Y. Zhu, Y. Zhang, Y. Liu, L. Li, *Mater. Res. Express* 6 (2019) 075067.
- [156] J. Zhang, R. Shi, Y. Zhu, Y. Liu, Y. Zhang, S. Li, L. Li, *ACS Appl. Mater. Interfaces* 10 (2018) 24975–24980.
- [157] X. Ding, Y. Zhu, L. Wei, Y. Li, L. Li, *Energy* 55 (2013) 933–938.
- [158] H. Gao, Y. Shao, R. Shi, Y. Liu, J. Zhu, J. Liu, Y. Zhu, J. Zhang, L. Li, X. Hu, *ACS Appl. Mater. Interfaces* 12 (2020) 47684–47694.
- [159] Q. Dong, P. Song, J. Tan, X.M. Qin, C.J. Li, P. Gao, Feng Z.X., M. Calin, J. Eckert, *J. Alloys Compd.* 823 (2020) 153783.
- [160] X.M. Qin, J. Tan, C.J. Li, X.C. Wang, Y.H. Jiang, R. Zhou, *J. Alloys Compd.* 647 (2015) 204–208.
- [161] J. Tan, Y. Zhang, B.A. Sun, M. Stoica, C.J. Li, K.K. Song, U. Kühn, F.S. Pan, J. Eckert, *Appl. Phys. Lett.* 98 (2011) 151906.
- [162] J. Tan, Y. Zhang, M. Stoica, U. Kühn, N. Mattern, F.S. Pan, J. Eckert, *Intermetallics* 19 (2011) 567–571.
- [163] Q. Dong, Y.J. Pan, J. Tan, X.M. Qin, C.J. Li, P. Gao, Z.X. Feng, M. Calin, J. Eckert, *J. Alloys Compd.* 785 (2019) 422–428.
- [164] J. Tan, G. Wang, Z.Y. Liu, J. Bednarčík, Y.L. Gao, Q.J. Zhai, N. Mattern, J. Eckert, *Sci. Rep.* 4 (2014) 3897.
- [165] H.J. Lin, W.H. Wang, M. Zhu, *J. Non-Cryst. Solids* 358 (2012) 1387–1390.
- [166] A. Inoue, K. Ohtera, K. Kita, T. Masumoto, *Jpn. J. Appl. Phys.* 27 (1988) L2248–L2251.
- [167] T. Spassov, U. Köster, *J. Alloys Compd.* 287 (1999) 243–250.
- [168] T. Spassov, U. Köster, *J. Alloys Compd.* 279 (1998) 279–286.
- [169] S. Kalinichenko, L. Röntzschi, T. Riedl, T. Gemming, T. Weißgärtner, B. Kieback, *Int. J. Hydrogen Energy* 36 (2011) 1592–1600.
- [170] H.J. Lin, C. Zhang, H. Wang, L. Ouyang, Y. Zhu, L. Li, W. Wang, M. Zhu, *J. Alloys Compd.* 685 (2016) 272–277.
- [171] H.J. Lin, M. He, S.P. Pan, L. Gu, H.W. Li, H. Wang, L.Z. Ouyang, J.W. Liu, T.P. Ge, D.P. Wang, W.-H. Wang, E. Akiba, M. Zhu, *Acta Mater.* 120 (2016) 68–74.
- [172] H.J. Lin, L. He, P. Zhang, Z. Zhang, S. Pan, W. Li, *Intermetallics* 97 (2018) 22–26.
- [173] C. Xu, H.J. Lin, K. Edalati, W. Li, L. Li, Y. Zhu, *Scripta Mater.* 152 (2018) 137–140.
- [174] H.J. Lin, C. Xu, M. Gao, Z. Ma, Y. Meng, L. Li, X. Hu, Y. Zhu, S. Pan, W. Li, *Intermetallics* 108 (2019) 94–99.

- [175] Y. Jia, X. Chen, Q. Le, H. Wang, L. Bao, *J. Magnes. Alloy.* 8 (2020) 716–730.
- [176] Y. Wang, S. Jia, M. Wei, L. Peng, Y. Wu, X. Liu, *J. Magnes. Alloy.* 8 (2020) 396–413.
- [177] S. Halder, S. Bhuyan, R.N.P. Choudhary, *J. Magnes. Alloy.* 7 (2019) 628–636.
- [178] Q. Li, K.D. Xu, K.C. Chou, X.G. Lu, J.Y. Zhang, G.W. Lin, *Intermetallics* 15 (2007) 61–68.
- [179] Q. Li, J. Liu, Y. Liu, K.C. Chou, *Int. J. Hydrogen Energy* 35 (2010) 3129–3135.
- [180] Q. Li, J. Liu, K.C. Chou, G.W. Lin, K.D. Xu, *J. Alloys Compd.* 466 (2008) 146–152.
- [181] Z.P. Yang, Q. Li, X.J. Zhao, *J. Alloys Compd.* 558 (2013) 99–104.
- [182] C. Jiang, H. Wang, X. Chen, Y. Tang, Z. Lu, Y. Wang, Z. Liu, *Electrochim. Acta* 112 (2013) 535–540.
- [183] P.Liu P, H. Zhang, X.L. Cheng, Y.J. Tang, *Appl. Surf. Sci.* 371 (2016) 44–49.
- [184] Q. Li, X.G. Lu, K.C. Chou, K.D. Xu, J.Y. Zhang, S.L. Chen, *Int. J. Hydrogen Energy* 32 (2007) 1875–1884.
- [185] J. Meng, Y.B. Pan, Q. Luo, X.H. An, Y. Liu, Q. Li, K.C. Chou, *Int. J. Hydrogen Energy* 35 (2010) 8310–8316.